J. Fluid Mech. (2023), *vol*. 977, A1, doi:10.1017/jfm.2023.925

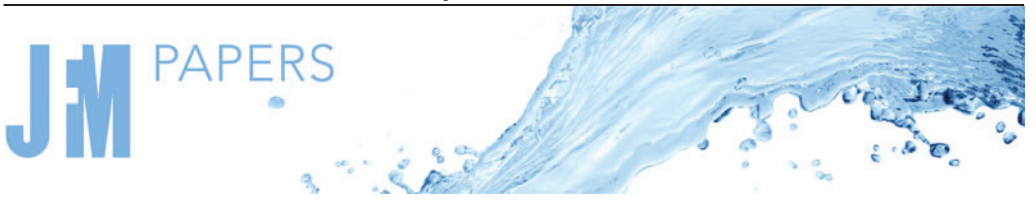

Flow-induced oscillations of pitching swept wings: stability boundary, vortex dynamics and force partitioning

Yuanhang Zhu[1],† **and Kenneth Breuer**[1]

[1]Center for Fluid Mechanics, School of Engineering, Brown University, Providence, RI 02912, USA

(Received 26 April 2023; revised 26 October 2023; accepted 29 October 2023)

We study experimentally the aeroelastic instability boundaries and three-dimensional vortex dynamics of pitching swept wings, with the sweep angle ranging from 0° to 25°. The structural dynamics of the wings are simulated using a cyber-physical control system. With a constant flow speed, a prescribed high inertia and a small structural damping, we show that the system undergoes a subcritical Hopf bifurcation to large-amplitude limit-cycle oscillations (LCOs) for all the sweep angles. The onset of LCOs depends largely on the static characteristics of the wing. The saddle-node point is found to change non-monotonically with the sweep angle, which we attribute to the non-monotonic power transfer between the ambient fluid and the elastic mount. An optimal sweep angle is observed to enhance the power extraction performance and thus promote LCOs and destabilize the aeroelastic system. The frequency response of the system reveals a structural-hydrodynamic oscillation mode for wings with relatively high sweep angles. Force, moment and three-dimensional flow structures measured using multi-layer stereoscopic particle image velocimetry are analysed to explain the differences in power extraction for different swept wings. Finally, we employ a physics-based force and moment partitioning method to correlate quantitatively the three-dimensional vortex dynamics with the resultant unsteady aerodynamic moment.

Key words: flow-structure interactions, vortex dynamics

1. Introduction

The fluid–structure interaction of elastically mounted pitching wings can lead to large-amplitude flow-induced oscillations under certain operating conditions. In extreme

† Email address for correspondence: yuanhang_zhu@brown.edu

cases, these flow-induced oscillations may affect structural integrity and even cause catastrophic aeroelastic failures (Dowell *et al.* 1989). On the other hand, however, hydrokinetic energy can be harnessed from these oscillations, providing an alternative solution for next-generation renewable energy devices (Xiao & Zhu 2014; Young, Lai & Platzer 2014; Boudreau *et al.* 2018; Su & Breuer 2019). Moreover, the aeroelastic/hydroelastic interactions of passively pitching wings/fins have important connections with animal flight (Wang 2005; Bergou, Xu & Wang 2007; Beatus & Cohen 2015; Wu, Nowak & Breuer 2019) and swimming (Long & Nipper 1996; Quinn & Lauder 2021), and understanding these interactions may aid further the design and development of flapping-wing micro air vehicles (Shyy *et al.* 2010; Jafferis *et al.* 2019) and oscillating-foil autonomous underwater vehicles (Zhong *et al.* 2021*b*; Tong *et al.* 2022).

Flow-induced oscillations of pitching wings originate from the two-way coupling between the structural dynamics of the elastic mount and the fluid force exerted on the wing. While the dynamics of the elastic mount can be approximated by a simple spring–mass–damper model, the fluid forcing term is usually found to be highly nonlinear due to the formation, growth and shedding of a strong leading-edge vortex (LEV) (McCroskey 1982; Dimitriadis & Li 2009; Mulleners & Raffel 2012; Eldredge & Jones 2019). Onoue *et al.* (2015) and Onoue & Breuer (2016) studied experimentally the flow-induced oscillations of a pitching plate whose structural stiffness, damping and inertia were defined using a cyber-physical system (§ 2.1; see also Hover, Miller & Triantafyllou 1997; Mackowski & Williamson 2011; Zhu, Su & Breuer 2020), and using this approach, identified a subcritical bifurcation to aeroelastic instability. The temporal evolution of the LEV associated with the aeroelastic oscillations was characterized using particle image velocimetry (PIV), and the unsteady flow structures were correlated with the unsteady aerodynamic moments using a potential flow model. Menon & Mittal (2019) studied numerically a similar problem, simulating an elastically mounted two-dimensional NACA 0015 aerofoil at Reynolds number 1000. An energy approach, which bridges prescribed sinusoidal oscillations and passive flow-induced oscillations, was employed to characterize the dynamics of the aeroelastic system. The energy approach maps out the energy transfer between the ambient flow and the elastic mount over a range of prescribed pitching amplitudes and frequencies, and unveils the system stability based on the sign of the energy gradient.

More recently, Zhu *et al.* (2020) characterized the effect of wing inertia on the flow-induced oscillations of pitching wings and the corresponding LEV dynamics. Two distinct oscillation modes were reported: (i) a structural mode, which occurred via a subcritical bifurcation and was associated with a high-inertia wing; and (ii) a hydrodynamic mode, which occurred via a supercritical bifurcation and was associated with a low-inertia wing. The wing was found to shed one strong LEV during each half-pitching cycle for the hydrodynamic mode, whereas a weak secondary LEV was also shed in the high-inertial structural mode.

These previous studies have demonstrated collectively that LEV dynamics plays an important role in shaping flow-induced oscillations and thus regulates the stability characteristics of passively pitching wings. However, these studies have focused only on studying the structural and flow dynamics of two-dimensional wings or aerofoils. The extent to which these important findings for two-dimensional wings hold in three dimensions remains unclear.

Swept wings are seen commonly for flapping-wing fliers and swimmers in nature (Ellington *et al.* 1996; Lentink *et al.* 2007; Borazjani & Daghooghi 2013; Bottom *et al.* 2016; Zurman-Nasution, Ganapathisubramani & Weymouth 2021), as well as on many

engineered fixed-wing flying vehicles. It is argued that wing sweep can enhance lift generation for flapping wings because it stabilizes the LEV by maintaining its size through spanwise vorticity transport – a mechanism similar to the lift enhancement mechanism of delta wings (Polhamus 1971). Chiereghin *et al.* (2020) found significant spanwise flow for a high-aspect-ratio plunging swept wing at sweep angle 40°. In another study, for the same sweep angle, attached LEVs and vortex breakdown were observed just like those on delta wings (Gursul & Cleaver 2019). Recent works have shown that the effect of wing sweep on LEV dynamics depends strongly on wing kinematics. Beem, Rival & Triantafyllou (2012) showed experimentally that for a plunging swept wing, the strong spanwise flow induced by the wing sweep is not sufficient for LEV stabilization. Wong, Kriegseis & Rival (2013) reinforced this argument by comparing the LEV stability of plunging and flapping swept wings, and showed that two-dimensional (i.e. uniform without any velocity gradient) spanwise flow alone cannot stabilize LEVs – there must be spanwise gradients in vorticity or spanwise flow so that vorticity can be convected or stretched. Wong & Rival (2015) demonstrated both theoretically and experimentally that the wing sweep improves relative LEV stability of flapping swept wings by enhancing the spanwise vorticity convection and stretching so as to keep the LEV size below a critical shedding threshold (Rival *et al.* 2014). Onoue & Breuer (2017) studied experimentally elastically mounted pitching unswept and swept wings, and proposed a universal scaling for the LEV formation time and circulation, which incorporated the effects of the pitching frequency, the pivot location and the sweep angle. The vortex circulation was demonstrated to be independent of the three-dimensional vortex dynamics. In addition, they concluded that the stability of the LEV can be improved by moderating the LEV circulation through vorticity annihilation, which is governed largely by the shape of the leading-edge sweep, agreeing with the results of Wojcik & Buchholz (2014). More recently, Visbal & Garmann (2019) studied numerically the effect of wing sweep on the dynamic stall of pitching three-dimensional wings, and reported that the wing sweep can modify the LEV structures and change the net aerodynamic damping of the wing. The effect of wing sweep on the LEV dynamics and stability, as one can imagine, will further affect the unsteady aerodynamic forces and thereby the aeroelastic response of pitching swept wings.

Another important flow feature associated with unsteady three-dimensional wings is the behaviour of the tip vortex (TV). Although the TV usually grows distinctly from the LEV for rectangular platforms (Taira & Colonius 2009; Kim & Gharib 2010; Hartloper, Kinzel & Rival 2013), studies have suggested that the TV is able to anchor the LEV in the vicinity of the wing tip, which delays LEV shedding (Birch & Dickinson 2001; Hartloper *et al.* 2013). Moreover, the TV has also been shown to affect the unsteady wake dynamics of both unswept and swept wings (Taira & Colonius 2009; Zhang *et al.* 2020*a*,*b*; Ribeiro *et al.* 2022; Son *et al.* 2022*a*; Son, Wang & Gursul 2022*b*). However, it remains elusive how the interactions between LEVs and TVs change with the wing sweep, and more importantly, how this change will in turn affect the response of aeroelastic systems.

To dissect the effects of complex vortex dynamics associated with unsteady wings/aerofoils, a physics-based force and moment partitioning method (FMPM) has been proposed (Quartapelle & Napolitano 1983; Zhang, Hedrick & Mittal 2015; Moriche, Flores & García-Villalba 2017; Menon & Mittal 2021*a*,*b*,*c*) (also known as the vortex force/moment map method; Li & Wu 2018; Li *et al.* 2020*a*). The method has attracted attention recently due to its high versatility for analysing a variety type of vortex-dominated flows. Under this framework, the Navier–Stokes equation is projected onto the gradient of an influence potential to separate the force contributions from the added-mass, vorticity-induced and viscous terms. It is particularly useful for analysing

vortex-dominated flows because the spatial distribution of the vorticity-induced forces can be visualized, enabling detailed dissections of aerodynamic loads generated by individual vortical structures. For two-dimensional aerofoils, Menon & Mittal (2021*c*) applied the FMPM and showed that the strain-dominated region surrounding the rotation-dominated vortices has an important role to play in the generation of unsteady aerodynamic forces. For three-dimensional wings, this method has been implemented to study the contributions of spanwise and cross-span vortices to the lift generation of rectangular wings (Menon, Kumar & Mittal 2022), the vorticity-induced force distributions on forward- and backward-swept wings at a fixed angle of attack (Zhang & Taira 2022) and the aerodynamic forces on delta wings (Li, Zhao & Graham 2020*b*). More recently, efforts have been made to apply the FMPM to the analysis of experimental data, in particular, flow fields obtained using PIV. Zhu *et al.* (2023) employed the FMPM to analyse the vortex dynamics of a two-dimensional wing pitching sinusoidally in a quiescent flow. Several practical issues in applying the FMPM to PIV data were discussed, including the effect of phase-averaging and potential error sources.

In this study, we apply the FMPM to three-dimensional flow field data measured using three-component PIV, and use the results to gain insight into the three-dimensional vortex dynamics and the corresponding unsteady forces acting on elastically mounted pitching swept wings. We extend the methodology developed in Zhu *et al.* (2020), and employ a layered stereoscopic PIV technique and the FMPM to quantify the three-dimensional vortex dynamics. In the following sections, we first introduce the experimental set-up and method of analysis (§ 2). The static force and moment coefficients of the wings are measured (§ 3.1) before we characterize the amplitude response (§ 3.2) and the frequency response (§ 3.3) of the system. Next, we associate the onset of flow-induced oscillations with the static characteristics of the wing (§ 3.4) and use an energy approach to explain the nonlinear stability boundaries (§ 3.5). The unsteady force and moment measurements, together with the three-dimensional flow structures (§ 3.6) are then analysed to explain the differences in power extraction for unswept and swept wings. Finally, we apply the FMPM to correlate quantitatively the three-dimensional vortex dynamics with the resultant unsteady aerodynamic moment (§ 3.7). All the key findings are summarized in § 4.

2. Methods

2.1. *Cyber-physical system and wing geometry*

We perform all the experiments in the Brown University free-surface water tunnel, which has test section $W \times D \times L = 0.8\,\mathrm{m} \times 0.6\,\mathrm{m} \times 4.0\,\mathrm{m}$. The turbulence intensity in the water tunnel is approximately 2 % at the velocity range tested in the present study. Free-stream turbulence plays a critical role in shaping small-amplitude laminar separation flutter (see Yuan *et al.* 2015). However, as we will show later, the flow-induced oscillations and the flow structures observed in the present study are of high amplitude and large size. Therefore, we do not expect the free-stream turbulence to play any significant role. Figure 1(*a*) shows a schematic of the experimental set-up. Unswept and swept NACA 0012 wings are mounted vertically in the tunnel, with an endplate on the top as a symmetry plane. The wing tip at the bottom does not have an endplate. The wings are connected to a six-axis force/moment transducer (ATI Delta IP65) via a wing shaft. The shaft further connects the transducer to an optical encoder (US Digital E3-2500) and a servo motor (Parker SM233AE) coupled with a gearbox (SureGear PGCN23-0525).

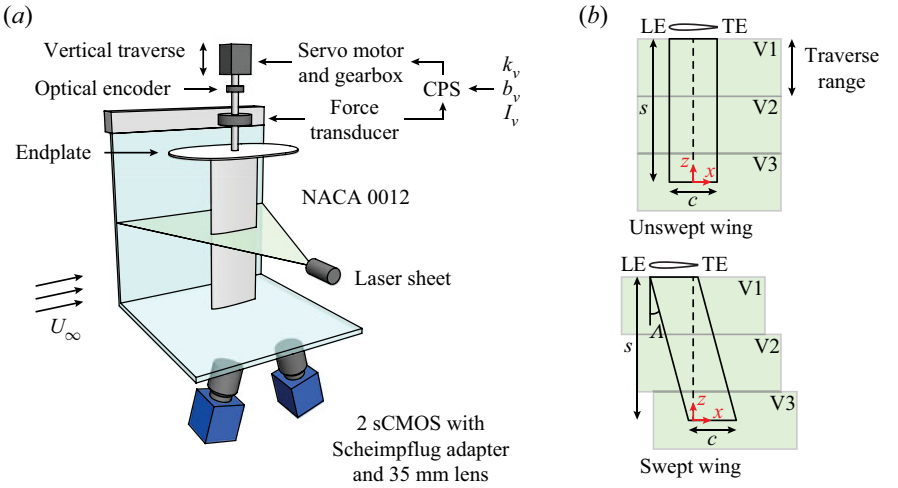

Figure 1. (*a*) A schematic of the experimental set-up. (*b*) Sketches of unswept and swept wings used in the experiments. The pivot axes are indicated by black dashed lines. The green panels represent volumes traversed by the laser sheet for three-dimensional phase-averaged stereoscopic PIV measurements.

We implement a cyber-physical system (CPS) to facilitate a wide structural parameter sweep (i.e. stiffness k, damping b, and inertia I) while simulating real aeroelastic systems with high fidelity. Details of the CPS have been discussed in Zhu *et al.* (2020), therefore only a brief introduction will be given here. In the CPS, the force/moment transducer measures the fluid moment M, and feeds the value to the computer via a data acquisition board (National Instruments PCIe-6353). This fluid moment is then added to the stiffness moment ($k\theta$) and the damping moment ($b\dot{\theta}$) obtained from the previous time step to get the total moment. Next, we divide this total moment by the desired inertia (I) to get the acceleration ($\ddot{\theta}$) at the present time step. This acceleration is then integrated once to get the velocity ($\dot{\theta}$), and twice to get the pitching angle (θ). This pitching angle signal is output to the servo motor via the same data acquisition board. The optical encoder, which is independent of the CPS, is used to measure and verify the pitching angle. At the next time step, the CPS recalculates the total moment based on the measured fluid moment and the desired stiffness and damping, and thereby continues the loop.

Our CPS control loop runs at frequency 4000 Hz, which is well beyond the highest Nyquist frequency of the aeroelastic system. Noise in the force/moment measurements can be a potential issue for the CPS. However, because we are using a position control loop, where the acceleration is integrated twice to get the desired position, our system is less susceptible to noise. Therefore, no filter is used within the CPS control loop. The position control loop also requires the pitching motor to follow the commanded position signal as closely as possible. This is achieved by carefully tuning the proportional–integral–derivative parameters of the pitching motor. The CPS does not rely on any additional tunable parameters other than the virtual inertia, damping and stiffness. We validate the system using 'ring-down' experiments, as shown in the appendix of Zhu *et al.* (2020). Moreover, as we will show later, the CPS results match remarkably well with prescribed experiments (§ 3.5), demonstrating the robustness of the system.

The unswept and swept wings used in the present study are sketched in figure 1(*b*). All the wings have span $s = 0.3$ m and chord length $c = 0.1$ m, which results in a physical aspect ratio $AR = 3$. However, the effective aspect ratio is 6 due to the existence of the

symmetry plane (i.e. the endplate). The minimum distance between the wing tip and the bottom of the water tunnel is approximately $1.5c$. The chord-based Reynolds number is defined as $Re \equiv \rho U_\infty c/\mu$, where U_∞ is the free-stream velocity, and ρ and μ are water density and dynamic viscosity, respectively. We set the free-stream velocity to be $U_\infty = 0.5\,\mathrm{m\,s^{-1}}$ for all the experiments (except for PIV measurements; see § 2.2), which results in a constant Reynolds number $Re = 50\,000$, matching the Re used in Zhu *et al.* (2020) to facilitate direct comparisons. For both unswept and swept wings, the leading edge (LE) and the trailing edge (TE) are parallel. Their pivot axes, represented by vertical dashed lines in the figure, pass through the mid-chord point $x/c = 0.5$ of the mid-span plane $z/s = 0.5$. We choose the current location of the pitching axis because it splits the swept wings into two equal-area sections (fore and aft). Moving the pitching axis or making it parallel to the leading edge presumably will result in different system dynamics, which will be investigated in future studies.

The sweep angle Λ, is defined as the angle between the leading edge and the vertical axis. Five wings, with $\Lambda = 0^\circ$ (unswept wing), 10°, 15°, 20° and 25° (swept wings), are used in the experiments. Further expanding the range of wing sweep presumably would bring more interesting fluid–structure interaction behaviours. However, as we will show in the later sections, there is already a series of rich (nonlinear) flow physics associated with the current set of unswept and swept wings. Our selection of the sweep angle is also closely related to the location of the pitching axis. Currently, the pitching axis passes the mid-chord at the mid-span. For a $\Lambda = 25^\circ$ wing, the trailing edge is already in front of the pitching axis at the wing root, and the leading edge is behind the pitching axis at the wing tip. Further increasing the sweep angle brings difficulties in physically pitching the wing for our existing set-up.

2.2. *Multi-layer stereoscopic PIV*

We use multi-layer phase-averaged stereoscopic PIV to measure the three-dimensional velocity field around the pitching wings. We lower the free-stream velocity to $U_\infty = 0.3\,\mathrm{m\,s^{-1}}$ to enable higher temporal measurement resolution. Consequently, the chord-based Reynolds number is decreased to $Re = 30\,000$. It has been shown by Zhu *et al.* (2020, see their appendix) that the variation of Re in the range 30 000–60 000 does not affect the system dynamics, as long as the parameters of interest are properly non-dimensionalized. The water flow is seeded using neutrally buoyant 50 µm silver-coated hollow ceramic spheres (Potters Industries) and illuminated using a horizontal laser sheet, generated by a double-pulse Nd:YAG laser (532 nm, Quantel EverGreen) with a LaVision laser guiding arm and collimator. Two sCMOS cameras (LaVision, 2560 × 2160 pixels) with Scheimpflug adapters (LaVision) and 35 mm lenses (Nikon) are used to capture image pairs of the flow field. These stereoscopic PIV image pairs are fed into the LaVision DaVis software (v.10) for velocity vector calculation using multi-pass cross-correlations (two passes at 64 × 64 pixels, two passes at 32 × 32 pixels, both with 50 % overlap).

To measure the two-dimensional, three-component (2D3C) velocity field at different spanwise layers, we use a motorized vertical traverse system with range 120 mm to raise and lower the testing rig (i.e. all the components connected by the shaft) in the z-axis (King, Kumar & Green 2018; Zhong *et al.* 2021*a*). Due to the limitation of the traversing range, three measurement volumes (figure 1(*b*), V1, V2 and V3) are needed to cover the entire wing span plus the wing tip region. For each measurement volume, the laser sheet is fixed at the top layer, and the rig is traversed upwards with step size 5 mm. Note that

the entire wing stays submerged, even at the highest traversing position, and for all wing positions, free surface effects are not observed. The top two layers of V1 are discarded as the laser sheet is too close to the endplate, which causes reflections. The bottom layer of V1 and the top layer of V2 overlap each other. The velocity fields of these two layers are averaged to smooth the interface between the two volumes. The interface between V2 and V3 is smoothed in the same way. For each measurement layer, we phase-average 1250 instantaneously measured 2D3C velocity fields over 25 cycles (i.e. 50 measurements per cycle) to eliminate any instantaneous variations of the flow field while maintaining the key coherent features across different layers. Finally, 71 layers of 2D3C velocity fields are stacked together to form a large volume of phase-averaged three-dimensional, three-component (3D3C) velocity field ($\sim 3c \times 3c \times 3.5c$). The velocity fields of three wing models ($\Lambda = 0^\circ$, 10° and 20°) are measured. For the two swept wings ($\Lambda = 10^\circ$ and 20°), the laser volumes are offset horizontally to compensate for the sweep angle (see the bottom image of figure 1*b*).

2.3. *Governing equations and non-dimensional parameters*

The one-degree-of-freedom aeroelastic system considered in the present study has a governing equation

$$I\ddot{\theta} + b\dot{\theta} + k\theta = M, \tag{2.1}$$

where θ, $\dot{\theta}$ and $\ddot{\theta}$ are the angular position, velocity and acceleration, respectively. Here, $I = I_p + I_v$ is the effective inertia, where I_p is the physical inertia of the wing, and I_v is the virtual inertia that we prescribe with the CPS. Because friction is negligible in our system, the effective structural damping b equals the virtual damping b_v in the CPS. Also, k is the effective torsional stiffness, and it equals the virtual stiffness k_v. Equation (2.1) resembles a forced torsional spring–mass–damper system, where the fluid moment M acts as a nonlinear forcing term. Following Onoue *et al.* (2015) and Zhu *et al.* (2020), we normalize the effective inertia, damping, stiffness and the fluid moment using the fluid inertia force to get the non-dimensional governing equation of the system:

$$I^*\ddot{\theta}^* + b^*\dot{\theta}^* + k^*\theta^* = C_M, \tag{2.2}$$

where

$$\left.\begin{gathered} \theta^* = \theta, \quad \dot{\theta}^* = \frac{\dot{\theta}c}{U_\infty}, \quad \ddot{\theta}^* = \frac{\ddot{\theta}c^2}{U_\infty^2}, \\ I^* = \frac{I}{0.5\rho c^4 s}, \quad b^* = \frac{b}{0.5\rho U_\infty c^3 s}, \quad k^* = \frac{k}{0.5\rho U_\infty^2 c^2 s}, \quad C_M = \frac{M}{0.5\rho U_\infty^2 c^2 s}. \end{gathered}\right\} \tag{2.3}$$

We should note that the inverse of the non-dimensional stiffness is equivalent to the Cauchy number $Ca = 1/k^*$, and the non-dimensional inertia I^* is analogous to the mass ratio between the wing and the surrounding fluid. We define the non-dimensional velocity as $U^* = U_\infty/(2\pi f_p c)$, where f_p is the measured pitching frequency. In addition to the aerodynamic moment, we also measure the aerodynamic forces that are normal and tangential to the wing chord, F_N and F_T, respectively. The resultant lift and drag forces are

$$\left.\begin{aligned} L &= F_N \cos\theta - F_T \sin\theta, \\ D &= F_N \sin\theta + F_T \cos\theta. \end{aligned}\right\} \tag{2.4}$$

We further normalize the normal force, tangential force, lift and drag to get the corresponding force coefficients

$$C_N = \frac{F_N}{0.5\rho U_\infty^2 cs}, \quad C_T = \frac{F_T}{0.5\rho U_\infty^2 cs}, \quad C_L = \frac{L}{0.5\rho U_\infty^2 cs}, \quad C_D = \frac{D}{0.5\rho U_\infty^2 cs}. \tag{2.5a–d}$$

2.4. *Force and moment partitioning method*

To apply the FMPM to three-dimensional PIV data, we first construct an influence potential that satisfies Laplace's equation and two different Neumann boundary conditions on the aerofoil and the outer boundary:

$$\nabla^2\phi = 0 \quad \text{and} \quad \frac{\partial\phi}{\partial \boldsymbol{n}} = \begin{cases} [(\boldsymbol{x} - \boldsymbol{x_p}) \times \boldsymbol{n}] \cdot \boldsymbol{e_z} & \text{on the aerofoil,} \\ 0 & \text{on the outer boundary,} \end{cases} \tag{2.6a,b}$$

where $\boldsymbol{n}$ is the unit vector normal to the boundary, $\boldsymbol{x} - \boldsymbol{x_p}$ is the location vector pointing from the pitching axis $\boldsymbol{x_p}$ towards location $\boldsymbol{x}$ on the aerofoil surface, and $\boldsymbol{e_z}$ is the spanwise unit vector (Menon & Mittal 2021*b*). This influence potential quantifies the spatial influence of any vorticity on the resultant force/moment. It is a function of only the aerofoil geometry and the pitching axis, and does not depend on the kinematics of the wing. Note that this influence potential should not be confused with the velocity potential from the potential flow theory. The boundary conditions of (2.6*a*,*b*) are specified for solving the influence field of the spanwise moment, and they will be different for solving the lift and drag influence fields. From the three-dimensional velocity data, we can calculate the Q field (Hunt, Wray & Moin 1988; Jeong & Hussain 1995)

$$Q = \tfrac{1}{2}(\|\boldsymbol{\Omega}\|^2 - \|\boldsymbol{S}\|^2), \tag{2.7}$$

where Q is the second invariant of the velocity gradient tensor, $\boldsymbol{\Omega}$ is the vorticity tensor and $\boldsymbol{S}$ is the strain-rate tensor. The vorticity-induced moment can be evaluated by

$$M_v = -2\rho \int_V Q\phi \, \mathrm{d}V, \tag{2.8}$$

where $\int_V$ represents the volume integral within the measurement volume. The spatial distribution of the vorticity-induced moment near the pitching wing can thus be represented by the moment density $-2Q\phi$ (i.e. the moment distribution field). In the present study, we focus on the vorticity-induced force (moment) as it has the most important contribution to the overall unsteady aerodynamic load in vortex-dominated flows. Other forces – including the added-mass force, the force due to viscous diffusion, the forces associated with irrotational effects and outer domain effects – are not considered although they can be estimated using the FMPM as well (Menon & Mittal 2021*b*). The contributions from these other forces, along with experimental errors, might result in a mismatch in the magnitude of the FMPM-estimated force and force transducer measurements, as shown by Zhu *et al.* (2023), and the exact source of this mismatch is under investigation.

3. Results and discussion

3.1. *Static characteristics of unswept and swept wings*

The static lift and moment coefficients C_L and C_M are measured for the unswept ($\Lambda = 0^\circ$) and swept ($\Lambda = 10^\circ$–25°) wings at $Re = 50\,000$, and the results are shown in figure 2. In

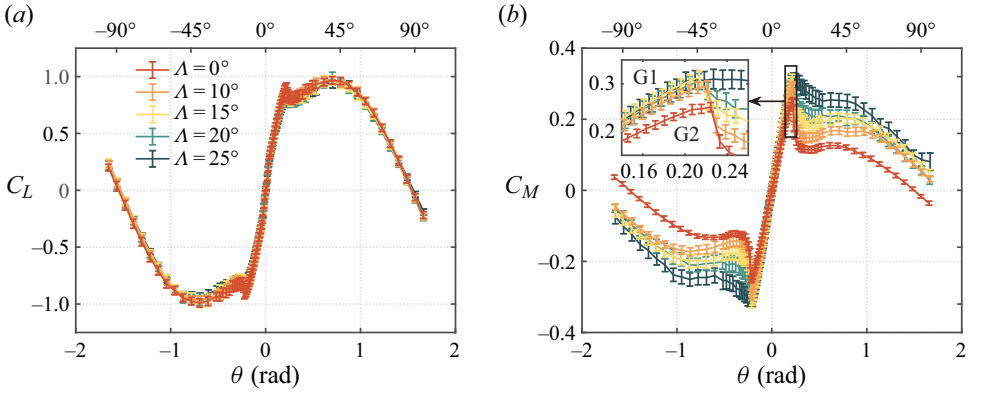

Figure 2. (*a*) Static lift coefficient and (*b*) moment coefficient of unswept and swept wings. Error bars denote standard deviations of the measurement over 20 seconds.

figure 2(*a*), we see that the static lift coefficient $C_L(\theta)$ has the same behaviour for all sweep angles, despite some minor variations for angles of attack higher than the static stall angle $\theta_s = 12^\circ$ (0.21 rad). The collapse of $C_L(\theta)$ across different swept wings agrees with the classic 'independence principle' (Jones 1947) (i.e. $C_L \sim \cos^2 \Lambda$) at relatively small sweep angles. Figure 2(*b*) shows that for any fixed angle of attack, the static moment coefficient C_M increases with the sweep angle Λ. This trend is most prominent when the angle of attack exceeds the static stall angle. The inset shows a zoom-in view of the static C_M for $\theta = 0.14$–0.26. It is seen that the C_M curves cluster into two groups, with the unswept wing ($\Lambda = 0^\circ$) being in group 2 (G2), and all the other swept wings ($\Lambda = 10^\circ$–25°) being in group 1 (G1). As we will show later, this grouping behaviour is closely related to the onset of flow-induced oscillations (§§ 3.2 and 3.4), and it is important for understanding the system stability. No hysteresis is observed for both static C_L and C_M, presumably due to free-stream turbulence in the water tunnel.

3.2. *Subcritical bifurcations to flow-induced oscillations*

We conduct bifurcation tests to study the stability boundaries of the elastically mounted pitching wings. Zhu *et al.* (2020) have shown that for unswept wings, the onset of limit-cycle oscillations (LCOs) is independent of the wing inertia and the bifurcation type (i.e. subcritical or supercritical). It has also been shown that the extinction of LCOs for subcritical bifurcations at different wing inertias occurs at a fixed value of the non-dimensional velocity U^*. For these reasons, we choose to focus on one high-inertia case ($I^* = 10.6$) in the present study. In the experiments, the free-stream velocity is maintained at $U_\infty = 0.5\,\mathrm{m\,s^{-1}}$. We fix the structural damping of the system at a small value, $b^* = 0.13$, keep the initial angle of attack at zero, and use the Cauchy number Ca as the control parameter. To test for the onset of LCOs, we begin the test with a high-stiffness virtual spring (i.e. low Ca) and increase Ca incrementally by decreasing the torsional stiffness k^*. We then reverse the operation to test for the extinction of LCOs and to check for any hysteresis. The amplitude response of the system, A, is measured as the peak absolute pitching angle (averaged over many pitching cycles). By this definition, A is half of the peak-to-peak amplitude. The divergence angle $\bar{A}$ is defined as the mean absolute pitching angle. Although all the divergence angles are shown to be positive, the wing can diverge to both positive and negative angles in experiments.

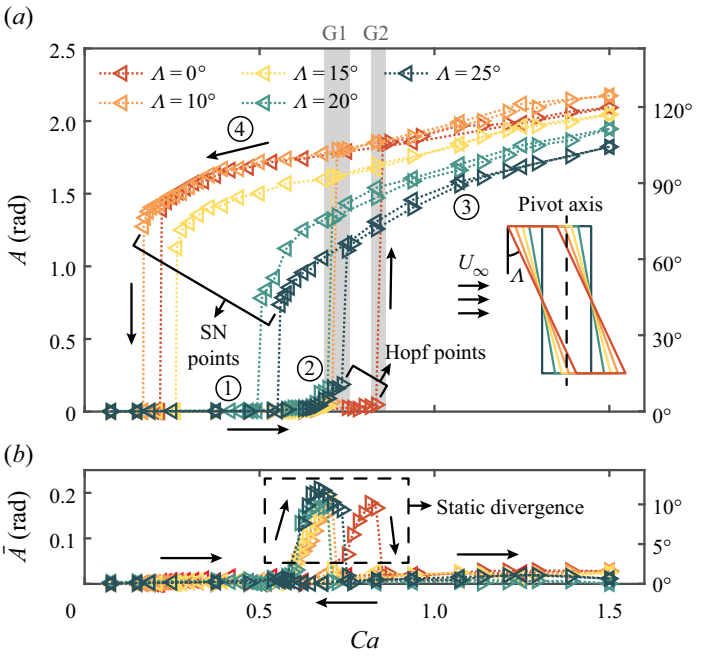

Figure 3. (*a*) Amplitude response and (*b*) static divergence for unswept and swept wings: ▷ indicates increasing *Ca*; ◁ indicates decreasing *Ca*. The inset illustrates the wing geometry and the pivot axis. The colours of the wings correspond to the colours of the amplitude and divergence curves in the figure.

Figure 3 shows the pitching amplitude response and the static divergence angle for swept wings with $\Lambda = 10^\circ$ to 25°. Data for the unswept wing ($\Lambda = 0^\circ$) are also replotted from Zhu *et al.* (2020) for comparison. It can be seen that the system first remains stable without any noticeable oscillations or divergence (regime ① in the figure) when *Ca* is small. In this regime, the high stiffness of the system is able to pull the system back to a stable fixed point despite any small perturbations. As we increase *Ca* further, the system diverges to a small static angle, where the fluid moment is balanced by the virtual spring. Presumably, this transition is triggered by free-stream turbulence, and both positive and negative directions are possible. Due to the existence of random flow disturbances and the decreasing spring stiffness, some small-amplitude oscillations around the static divergence angle start to emerge (regime ②). As *Ca* is increased further above a critical value (i.e. the Hopf point), the amplitude response of the system jumps abruptly into large-amplitude self-sustained LCOs, and the static divergence angle drops back to zero, indicating that the oscillations are symmetric about the zero angle of attack. The large-amplitude LCOs are observed to be near-sinusoidal and have a dominant characteristic frequency. After the bifurcation, the amplitude response of the system continues to increase with *Ca* (regime ③). We then decrease *Ca* and find that the large-amplitude LCOs persist even when *Ca* is decreased below the Hopf point (regime ④). Finally, the system drops back to the stable fixed point regime via a saddle-node (SN) point. A hysteretic bistable region is thus created in between the Hopf point and the SN point – a hallmark of a subcritical Hopf bifurcation. In the bistable region, the system features two stable solutions – a stable fixed point (regime ①) and a stable LCO (regime ④) – as well as an unstable LCO solution, which is not observable in experiments (Strogatz 1994).

We observe that the Hopf points of unswept and swept wings can be divided roughly into two groups (figure 3, G1 and G2), with the unswept wing ($\Lambda = 0^\circ$) being in G2, and all the other swept wings ($\Lambda = 10^\circ$–25°) being in G1, which agrees with the trend observed in figure 2(*b*) for the static moment coefficient. This connection will be discussed further in § 3.4. It is also seen that as the sweep angle increases, the LCO amplitude at the SN point decreases monotonically. However, the *Ca* at which the SN point occurs first extends towards a lower value ($\Lambda = 0^\circ \rightarrow 10^\circ$) but then moves back towards a higher *Ca* ($\Lambda = 10^\circ \rightarrow 25^\circ$). This indicates that increasing the sweep angle first destabilizes the system from $\Lambda = 0^\circ$ to 10°, and then restabilizes it from $\Lambda = 10^\circ$ to 25°. This non-monotonic behaviour of the SN point will be revisited from a perspective of energy in § 3.5. The pitching amplitude response, A, follows a similar non-monotonic trend. Between $\Lambda = 0^\circ$ and 10°, A is slightly higher at higher *Ca* values for the $\Lambda = 10^\circ$ wing, whereas between $\Lambda = 10^\circ$ and 25°, A decreases monotonically, indicating that a higher sweep angle is not able to sustain LCOs at higher amplitudes. The non-monotonic behaviours of the SN point and the LCO amplitude both suggest that there exists an optimal sweep angle $\Lambda = 10^\circ$ that promotes flow-induced oscillations of pitching swept wings.

3.3. *Frequency response of the system*

The characteristic frequencies of the flow-induced LCOs observed in figure 3 provide us with more information about the driving mechanism of the oscillations. Figure 4(*a*) shows the measured frequency response f_p^* as a function of the calculated natural (structural) frequency f_s^* and sweep angle. In the figure, $f_p^* = f_p c/U_\infty$ and $f_s^* = f_s c/U_\infty$, where f_p is the measured pitching frequency, and

$$f_s = \frac{1}{2\pi}\sqrt{\frac{k}{I} - \left(\frac{b}{2I}\right)^2} \tag{3.1}$$

is the structural frequency of the system (Rao 1995). We observe that for all the wings tested in the experiments and over most of the regimes tested, the measured pitching frequency f_p^* locks onto the calculated structural frequency f_s^*, indicating that the oscillations are dominated by the balance between the structural stiffness and inertia. These oscillations, therefore, correspond to the structural mode reported by Zhu *et al.* (2020), and feature characteristics of high-inertial aeroelastic instabilities. We can decompose the moments experienced by the wing into the inertial moment $I^*\ddot{\theta}^*$, the structural damping moment $b^*\dot{\theta}^*$, the stiffness moment $k^*\theta^*$ and the fluid moment C_M. As an example, for the $\Lambda = 10^\circ$ wing pitching at $f_s^* = 0.069$ (i.e. the filled orange triangle in figure 4*a*), these moments are plotted in figure 4(*b*). We see that for the structural mode, the stiffness moment is balanced mainly by the inertial moment, while the structural damping moment and the fluid moment remain relatively small.

In addition to the structural mode, Zhu *et al.* (2020) also observed a hydrodynamic mode, which corresponds to a low-inertia wing. In the hydrodynamic mode, the oscillations are dominated by the fluid forcing, so that the measured pitching frequency f_p^* stays relatively constant for a varying *Ca*. In figure 4(*a*), we see that for the $\Lambda = 20^\circ$ and 25° wings, f_p^* flattens near the saddle-node boundary. This flattening trend shows an emerging fluid-dominated time scale, resembling a hydrodynamic mode despite the high wing inertia. Taking $\Lambda = 20^\circ$, $f_s^* = 0.068$ (i.e. the filled green diamond in figure 4*a*) as an example, we can examine the different contributions to the pitching moments in figure 4(*c*). It is observed that in this oscillation mode, the stiffness moment balances both the inertial

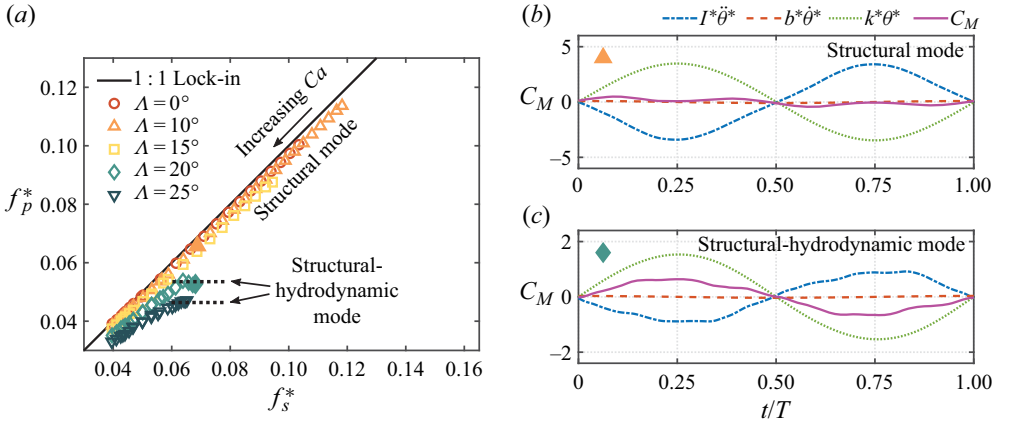

Figure 4. (*a*) Frequency response of unswept and swept wings. (*b*,*c*) Force decompositions of the structural mode and the structural-hydrodynamic mode, corresponding to the filled orange triangle and the filled green diamond shown in (*a*), respectively. Note that $t/T = 0$ corresponds to $\theta = 0$.

moment and the fluid moment. This is different from both the structural mode and the hydrodynamic mode, and for this reason, we define this hybrid oscillation mode as the structural-hydrodynamic mode.

There are currently no quantitative descriptions of the structural-hydrodynamic mode. However, it can be identified qualitatively as when the pitching frequency of a (1 : 1 lock-in) structural mode flattens as the natural (structural) frequency increases. Based on the observations in the present study, we believe that this mode is not a fixed fraction of the structural frequency. Instead, the frequency response shows a mostly flat trend (figure 4*a*, green and dark green curves) at high f_s^*, indicating an increasingly dominating fluid forcing frequency. For a structural mode, the oscillation frequency locks onto the natural frequency due to the high inertial moment. However, as the sweep angle increases, the fluid moment also increases (see also figure 8*a*). The structural-hydrodynamic mode emerges as the fluid forcing term starts to dominate in the nonlinear oscillator.

For a fixed structural frequency f_s^*, as the sweep angle increases, the measured pitching frequency f_p^* deviates from the 1 : 1 lock-in curve and moves to lower frequencies. This deviation suggests a growing added-mass effect, as the pitching frequency satisfies $f_p \sim \sqrt{1/(I + I_{add})}$. Because the structural inertia I is prescribed, a decreasing f_p suggests an increasing added-mass inertia I_{add}. This is expected because of the way we pitch the wings in the experiments (see the inset of figure 3). As Λ increases, the accelerated fluid near the wing root and the wing tip produces more moments due to the increase of the moment arm, which amplifies the added-mass effect. The peak added-mass moment is estimated to be approximately 2 %, 3 % and 5 % of the peak total moment for the $\Lambda = 0°$, 10° and 20° wings, respectively. Because this effect is small compared to the structural and vortex-induced forces, we will not quantify further this added-mass effect in the present study, but will leave it for future work.

3.4. *Onset of flow-induced oscillations*

In figure 3, we have observed that the Hopf point of unswept and swept wings can be divided roughly into two groups (figure 3, G1 and G2). In this subsection, we explain this phenomenon. Figures 5(*a*,*b*) show the temporal evolution of the pitching angle $\theta(t)$,

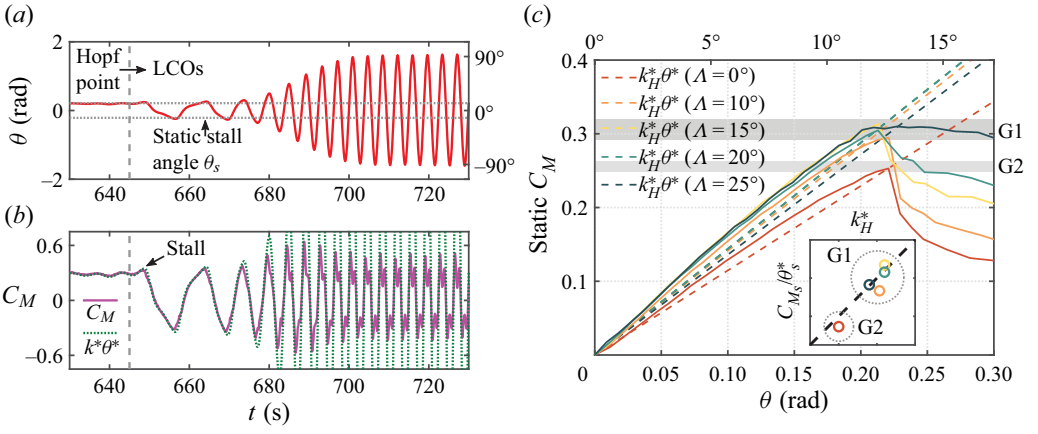

Figure 5. Temporal evolution of (*a*) the pitching angle θ, and (*b*) the fluid moment C_M and the stiffness moment $k^*\theta^*$ near the Hopf point for the $\Lambda = 15°$ swept wing. The vertical grey dashed line indicates the time instant ($t = 645$ s) at which Ca is increased above the Hopf point. (*c*) Static moment coefficients of unswept and swept wings. Inset: the predicted Hopf point based on the static stall angle and the corresponding moment C_{M_s}/θ_s^* versus the measured Hopf point k_H^*. The black dashed line shows a 1 : 1 scaling.

the fluid moment $C_M(t)$ and the stiffness moment $k^*\theta^*(t)$ for the $\Lambda = 15°$ swept wing as the Cauchy number is increased past the Hopf point. We see that the wing undergoes small-amplitude oscillations around the divergence angle just prior to the Hopf point ($t <$ 645 s). The divergence angle is lower than the static stall angle θ_s, so we know that the flow stays mostly attached, and the fluid moment C_M is balanced by the stiffness moment $k^*\theta^*$ (figure 5*b*). When the Cauchy number $Ca = 1/k^*$ is increased above the Hopf point (figure 5*a*, $t >$ 645 s), $k^*\theta^*$ is no longer able to hold the pitching angle below θ_s. Once the pitching angle exceeds θ_s, stall occurs and the wing experiences a sudden drop in C_M. The stiffness moment $k^*\theta^*$ loses its counterpart and starts to accelerate the wing to pitch towards the opposite direction. This acceleration introduces unsteadiness to the system, and the small-amplitude oscillations transition gradually to large-amplitude LCOs over the course of several cycles, until the inertial moment kicks in to balance $k^*\theta^*$ (see also figure 4*b*). This transition process confirms the fact that the onset of large-amplitude LCOs depends largely on the static characteristics of the wing – the LCOs are triggered when the static stall angle is exceeded.

The triggering of flow-induced LCOs starts from θ exceeding the static stall angle after k^* is decreased below the Hopf point, causing C_M to drop below $k^*\theta^*$. At this value of k^*, the slope of the static stall point should be equal to the stiffness at the Hopf point, k_H^* (i.e. $C_{M_s} = k_H^*\theta^*$, where C_{M_s} is the static stall moment). This argument is verified by figure 5(*c*), in which we replot the static moment coefficients of unswept and swept wings from figure 2(*b*) (error bars omitted for clarity), together with the corresponding $k_H^*\theta^*$. We see that the $k_H^*\theta^*$ lines all pass approximately through the static stall points (θ_s^*, C_{M_s}) of the corresponding Λ. Note that the $k_H^*\theta^*$ values for $\Lambda = 15°$ and 20° overlap each other. Similar to the trend observed for the Hopf point in figure 3, the static stall moment C_{M_s} can also be divided into two groups, with the unswept wing ($\Lambda = 0°$) being in G2, and all the other wings ($\Lambda = 10°$–$25°$) being in G1 (see also figure 2*b*). The inset compares the predicted Hopf point C_{M_s}/θ_s^* with the measured Hopf point k_H^*, and we see that the data follow closely a 1 : 1 relationship. This reinforces the argument that the onset

of flow-induced LCOs is shaped by the static characteristics of the wing, and that this explanation applies to both unswept and swept wings.

It is worth noting that Negi, Hanifi & Henningson (2021) performed global linear stability analysis on an aeroelastic wing and showed that the aeroelastic instability is triggered by a zero-frequency linear divergence mode. This agrees in part with our experimental observation that the flow-induced oscillations emerge from the static divergence state. However, as we have discussed in this subsection, the onset of large-amplitude aeroelastic oscillations in our system occurs when the divergence angle exceeds the static stall angle, whereas no stall is involved in the study of Negi *et al.* (2021). In fact, Negi *et al.* (2021) focused on laminar separation flutter, where the pitching amplitude is small ($A \sim 6^\circ$). In contrast, we focus on large-amplitude ($45^\circ < A < 120^\circ$) flow-induced oscillations.

3.5. *Power coefficient map and system stability*

In this subsection, we analyse the stability of elastically mounted unswept and swept wings from the perspective of energy transfer. Menon & Mittal (2019) and Zhu *et al.* (2020) have shown numerically and experimentally that the flow-induced oscillations of elastically mounted wings can sustain only when the net energy transfer between the ambient fluid and the elastic mount equals zero. To map out this energy transfer for a large range of pitching frequencies and amplitudes, we prescribe the pitching motion of the wing using a sinusoidal profile

$$\theta = A \sin(2\pi f_p t), \tag{3.2}$$

where $0 \leq A \leq 2.5$ rad and $0.15\,\text{Hz} \leq f_p \leq 0.6\,\text{Hz}$. The fluid moment C_M measured with these prescribed sinusoidal motions can be correlated directly to those measured in the passive flow-induced oscillations because the flow-induced oscillations are near-sinusoidal (see § 3.2, and figure 5*a*, $t > 700$ s). By integrating the governing equation of the passive system (2.2) over $n = 20$ cycles and taking the cycle average (Zhu *et al.* 2020), we can get the power coefficient of the system:

$$C_p = \frac{f_p^*}{n} \int_{t_0}^{t_0+nT} (C_M \dot{\theta}^* - b^* \dot{\theta}^{*2})\, \mathrm{d}t^*, \tag{3.3}$$

where t_0 is the starting time, T is the pitching period and $t^* = tU_\infty/c$ is the non-dimensional time. In this equation, the $C_M\dot{\theta}^*$ term represents the power injected into the system from the free-stream flow, whereas the $b^*\dot{\theta}^{*2}$ term represents the power dissipated by the structural damping of the elastic mount. The power coefficient maps of unswept and swept wings are shown in figures 6(*a–e*). In these maps, orange regions correspond to $C_p > 0$, where the power injected by the ambient flow is higher than that dissipated by the structural damping. On the contrary, $C_p < 0$ in the blue regions. The coloured dashed lines indicate the $C_p = 0$ contours, where the power injection balances the power dissipation, and the system is in equilibrium. The $C_p = 0$ equilibrium boundary can be divided into three branches. Zhu *et al.* (2020) have shown that for unswept wings, the top branch corresponds to a stable LCO solution for the structural oscillation mode, the middle branch represents an unstable LCO solution for the structural mode but a stable LCO solution for the hydrodynamic mode, and the bottom branch is a fixed point solution.

To correlate the power coefficient maps of prescribed oscillations with the stability boundaries of flow-induced oscillations, we overlay the bifurcation diagrams of the passive system from figure 3 onto figures 6(*a–e*). The measured pitching frequencies f_p are used to calculate the non-dimensional velocity U^* for large-amplitude LCOs (filled triangles).

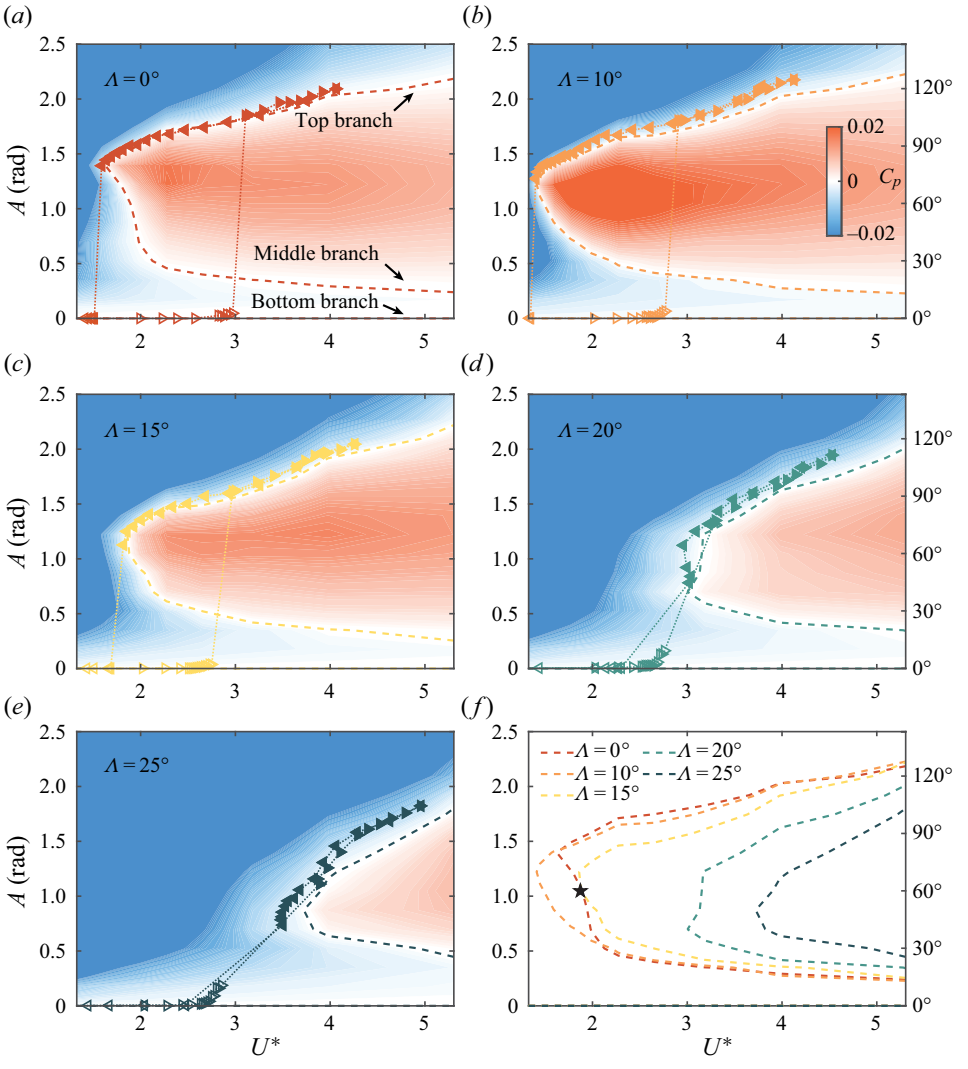

Figure 6. (*a–e*) Power coefficient maps of prescribed sinusoidal oscillations overlaid by the bifurcation diagrams of elastically mounted unswept and swept wings: ▷ indicates increasing *Ca*; ◁ indicates decreasing *Ca*. (*f*) Neutral power transfer curves for unswept and swept wings. The black star represents the case $U^* = 1.87$ ($f_p^* = 0.085$), $A = 1.05$ (60°), where stereo PIV measurements are taken.

Because it is difficult to measure frequencies of fixed points and small-amplitude oscillations, we use the calculated structural frequency f_s to evaluate U^* for non-LCO data points (hollow triangles). Figures 6(*a–e*) show that for all the wings tested, the flow-induced large-amplitude LCOs match well with the top branch of the $C_p = 0$ curve, indicating the broad applicability of the energy approach for both unswept and swept wings, and confirming that this instability is a structural mode, as seen in the frequency response (figure 4*a*). This correspondence was also observed by Menon & Mittal (2019) and Zhu *et al.* (2020), and is expected for instabilities that are well described by sinusoidal motions (Morse & Williamson 2009). The small discrepancies for large sweep angles can be attributed to the low C_p gradient near $C_p = 0$. The junction between the top and the

middle $C_p = 0$ branches, which corresponds to the SN point, stays relatively sharp for $\Lambda = 0°$–$15°$, and becomes smoother for $\Lambda = 20°$–$25°$. These smooth turnings result in a smooth transition from the structural mode to the hydrodynamic mode, giving rise to the structural-hydrodynamic mode discussed in § 3.3.

The $C_p = 0$ curves for $\Lambda = 0°$–$25°$ are summarized in figure 6(f). It is seen that the trend of the top branch is similar to that observed in figure 3 for large-amplitude LCOs. The location of the junction between the top branch and the middle branch changes non-monotonically with Λ, which accounts for the non-monotonic behaviour of the saddle-node point. In addition, figures 6(a–e) show that the maximum power transfer from the fluid also has a non-monotonic dependency on the sweep angle (see the shade variation of the positive C_p regions as a function of the sweep angle), with an optimal sweep angle at $\Lambda = 10°$, which might inspire future designs of higher efficiency oscillating-foil energy harvesting devices.

3.6. *Force, moment and three-dimensional flow structures*

In the previous subsection, § 3.5, we have established the connection between prescribed oscillations and flow-induced instabilities using the energy approach. However, the question remains as to what causes the differences in the power coefficients measured for prescribed pitching wings with different sweep angles (figure 6). In this subsection, we analyse the aerodynamic force, moment and corresponding three-dimensional flow structures to gain more insights. We focus on one pitching case, $A = 1.05$ (60°) and $f_p^* = 0.085$ (i.e. the black star on figure 6f), and three sweep angles, $\Lambda = 0°$, 10° and 20°. This particular pitching kinematic is selected because it sits right on the $C_p = 0$ curve for $\Lambda = 0°$ but in the positive C_p region for $\Lambda = 10°$ and in the negative C_p region for $\Lambda = 20°$ (see figures 6a,b,d,f).

Phase-averaged coefficients of the aerodynamic moment C_M, the normal force C_N, the tangential force C_T, the lift force C_L and the drag force C_D, are plotted in figures 7(a–c). Similar to the three-dimensional velocity fields, the moment and force measurements are phase-averaged over 25 cycles. We see that the moment coefficient (figure 7a) behaves differently for different sweep angles, whereas the shape of other force coefficients (figures 7b,c) does not change with sweep angle, resembling the trend observed in the static measurements (figure 2). The observation that the wing sweep ($\Lambda = 0°$ to 25°) has minimal effects on the aerodynamic force generation is non-intuitive, as one would assume that the sweep-induced spanwise flow can enhance spanwise vorticity transport in the LEV and thereby alter the LEV stability as well as the resultant aerodynamic load. However, our measurements show the opposite, a result that is backed up by the experiments of heaving (plunging) swept wings by Beem *et al.* (2012) ($\Lambda = 0°$ to 45°) and Wong *et al.* (2013) ($\Lambda = 0°$ and ±45°), simulations of pitching swept wings by Visbal & Garmann (2019) ($\Lambda = 0°$ to 30°) and simulations of fin-like pitch–heave swept wings by Zurman-Nasution *et al.* (2021) ($\Lambda = 0°$ to 40°), where the spanwise flow has been shown to exist but to have no effect on the aerodynamic force. We also analyse aerodynamic forces for different sweep angles and other wing kinematics, and observe similar results (not shown in this paper). The collapse of the normal force C_N at different sweep angles suggests that the wing sweep regulates the aerodynamic moment C_M by changing the moment arm d_M as $C_M = C_N d_M$. This argument will be revisited later when we discuss the LEV and TV dynamics.

Figure 7(a) shows that as the sweep angle increases, the moment coefficient C_M peaks at a later time in the cycle, and has an increased maximum value. To analyse further

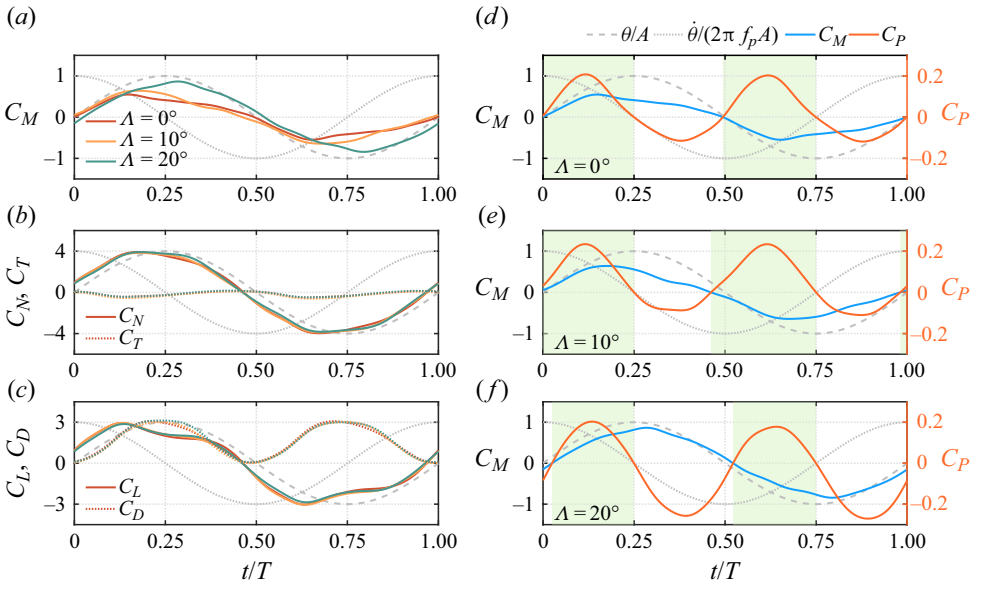

Figure 7. (*a*) Phase-averaged aerodynamic moment coefficients C_M, and (*b*,*c*) force coefficients C_N, C_T, C_L and C_D, measured at $f_p^* = 0.085$, $A = 1.05$ (60°) for the $\Lambda = 0°$, 10° and 20° wings, corresponding to the black star case in figure 6(*f*). (*d–f*) Phase-averaged moment coefficients C_M and power coefficients C_P for $\Lambda = 0°$, 10° and 20°. Green panels represent positive power input regions, where $C_P > 0$. Grey dashed lines and dotted lines represent the normalized pitching angle θ/A and pitching velocity $\dot{\theta}/(2\pi f_p A)$, respectively. Note that $t/T = 0$ corresponds to $\theta = 0$ (see the grey dashed curve).

C_M and its effects on the power coefficient C_P for different wings sweeps, we compare C_M and C_P for $\Lambda = 0°$, 10° and 20° in figures 7(*d–f*), respectively. Note that here we define the power coefficient as $C_P = C_M\dot{\theta}^*$, which is different from (3.3) in a way that this C_P is time-dependent instead of cycle-averaged, and that the power dissipated by the structure, $b^*\dot{\theta}^{*2}$, is not considered (this power dissipation is small because a small b^* is used in the experiments). The normalized pitching angle θ/A and pitching velocity $\dot{\theta}/(2\pi f_p A)$ are also plotted for reference. We see that at the beginning of the cycle ($0 \leq t/T < 0.15$), $C_M(t/T)$ grows near-linearly for all three wings. Because $\dot{\theta} > 0$ for the first quarter-cycle, the x-intercept of C_M determines the starting point of the positive $C_P(t/T)$ region, corresponding to the left edge of the green panels in the plots. The $C_P > 0$ region starts at $t/T = 0$ for the unswept wing as C_M has a near-zero y-intercept. For the $\Lambda = 10°$ swept wing, because C_M has a small positive y-intercept, the $C_P > 0$ region starts even before $t/T = 0$. On the contrary, the $C_P > 0$ region starts after $t/T = 0$ for the $\Lambda = 20°$ swept wing due to a small negative y-intercept of C_M. Owing to the combined effect of an increasing C_M and a decreasing $\dot{\theta}$, the power coefficient peaks at approximately $t/T = 0.125$ for all the wings. The maximum C_P of the $\Lambda = 10°$ wing is slightly higher than that of the other two wings, due to a slightly higher C_M.

As the pitching cycle continues, $C_M(t/T)$ peaks at approximately $t/T = 0.15$, 0.17 and 0.28 for $\Lambda = 0°$, 10° and 20°, respectively. The pitch reversal occurs at $t/T = 0.25$, where θ reaches its maximum and $\dot{\theta}$ switches its sign to negative. Because the pitching velocity is now negative, the green panels terminate as C_P drops below zero, suggesting that C_M starts to dissipate energy into the ambient fluid. However, because C_M continues to grow after $t/T = 0.25$ for the $\Lambda = 20°$ wing, it generates a much more negative C_P as compared

to the wings with a lower sweep angle. Figure 7(*a*) shows that C_M decreases faster for the $\Lambda = 10^\circ$ wing than for the unswept wing at $0.25 \leq t/T < 0.5$. This difference results in a less negative C_P for the $\Lambda = 10^\circ$ wing as compared to the $\Lambda = 0^\circ$ wing. The faster decrease of C_M for the $\Lambda = 10^\circ$ wing also makes it the first to switch back to positive power generation, where C_M and $\dot{\theta}$ are both negative. The same story repeats after $t/T = 0.5$ due to the symmetry of the pitching cycle. In summary, we see that subtle differences in the alignment of C_M and $\dot{\theta}$ can result in considerable changes of C_P for different sweep angles. The start of the $C_P > 0$ region is determined by the phase of C_M, whereas the termination of the $C_P > 0$ region depends on $\dot{\theta}$. A non-monotonic duration of the $C_P > 0$ region (i.e. the size of the green panels) is observed as the sweep angle increases. The cycle-averaged power coefficient, which dictates the stability of aeroelastic systems (see § 3.5), is regulated by both the amplitude and phase of the aerodynamic moment.

Next, we analyse the effect of wing sweep on the LEV and TV dynamics, and the resultant impact on the aerodynamic moment. Figure 8(*a*) shows the moment measurements, figures 8(*b–d*) show the phase-averaged three-dimensional flow structures at $t_1/T = 0.14$, $t_2/T = 0.22$ and $t_3/T = 0.30$, and figures 8(*e–g*) show the corresponding LEV and TV geometries for the $\Lambda = 0^\circ$, 10° and 20° wings. The three equally spaced time instants $t_1/T = 0.14$, $t_2/T = 0.22$ and $t_3/T = 0.30$ are selected because they correspond to the times of the formation, growth and shedding of the LEV. The three-dimensional flow structures are visualized using iso-Q surfaces with value $50\,\mathrm{s}^{-2}$ and coloured by the non-dimensional spanwise vorticity $\omega_z c/U_\infty$. In this view, the leading edge of the wing is pitching towards us, but for clarity, the flow field is always plotted with the coordinate system oriented so that the chord line is aligned with the x-axis.

The initial linear growth of the moment coefficient before t_1/T for all three wings corresponds to the formation of a strong LEV, as depicted in figures 8(*b–d*) at $t_1/T = 0.14$, which brings the lift and moment coefficients above the static stall limit. At this stage, we see that the structure of the LEV is similar across different wing sweeps, despite some minor variations near the wing tip. For the unswept wing, the LEV stays mostly attached along the wing span, whereas for the two swept wings, the LEV starts to detach near the tip region (see the small holes on the feeding shear layer near the wing tip). A positive vortex tube on the surface near the trailing edge is observed for all three wings, along with the negative vortex tubes shed from the trailing edge. We also observe a streamwise-oriented TV wrapping over the wing tip, and this TV grows stronger with the sweep angle, presumably due to the higher tip velocity associated with the larger wing sweep. Another possible cause for a stronger TV at a higher sweep angle is that the effective angle of attack becomes higher at the wing tip as the wing sweep increases.

The tracking of the vortex geometry (figures 8*e–g*) provides a more quantitative measure to analyse the LEV and TV dynamics. We see that at $t_1/T = 0.14$, the LEVs for all three wings are mostly aligned with the leading edge except for the tip region ($z/c = 0$). For the two swept wings, the LEV also stays closer to the leading edge near the wing root ($z/c = 3$). Due to the high wing sweep of the $\Lambda = 20^\circ$ wing, a small portion of the LEV falls behind the pivot axis, presumably contributing to a negative moment. However, the mean distance between the LEV and the pivot axis (i.e. the LEV moment arm) stays approximately constant across different wing sweeps, potentially explaining the agreement between the C_M for different wings during the linear growth region. On the other hand, the TV moves downstream as the wing sweep increases due to the wing geometry. For the unswept wing and the $\Lambda = 10^\circ$ swept wing, the majority of the TV stays behind the pivot axis. For the $\Lambda = 20^\circ$ swept wing, the TV stays entirely behind the pivot axis. As a

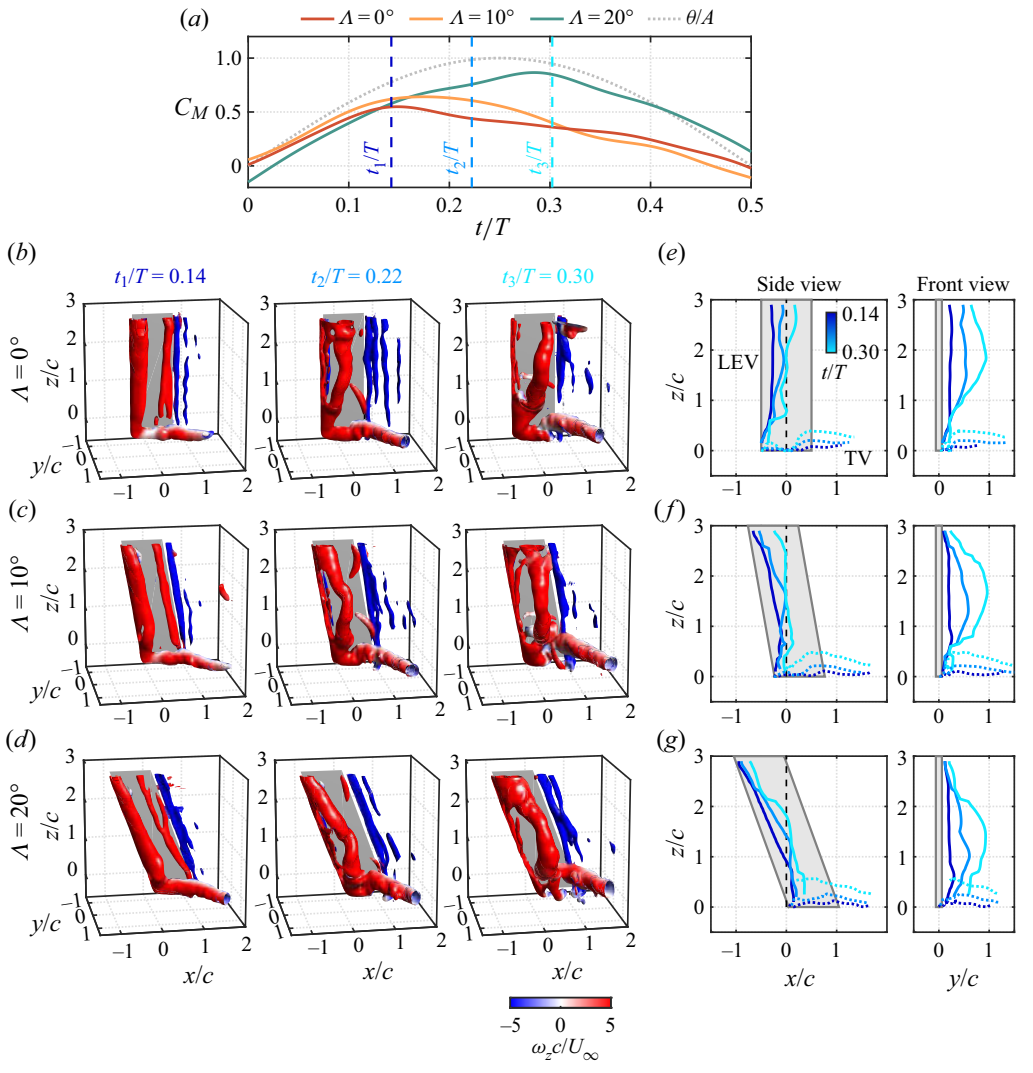

Figure 8. (*a*) Moment coefficients replotted from figure 7(*a*) for a half pitching cycle. Three representative time instants, $t_1/T = 0.14$, $t_2/T = 0.22$ and $t_3/T = 0.30$, are selected for studying the evolution of the LEV and TV. (*b–d*) Phase-averaged three-dimensional flow structures for the $\Lambda = 0°$ unswept wing, and the $\Lambda = 10°$ and $\Lambda = 20°$ swept wings. The flow structures are visualized with iso-Q surfaces ($Q = 50\,\mathrm{s}^{-2}$) and coloured by the non-dimensional spanwise vorticity $\omega_z c/U_\infty$. All the flow fields are rotated by the pitching angle to keep the wing at a zero angle of attack for better visualization of the flow structures. Movie 1, capturing the three-dimensional flow structures for the entire pitching cycle, can be found in the supplementary material available at https://doi.org/10.1017/jfm.2023.925. (*e–g*) Side views and front views of the corresponding three-dimensional LEV and TV geometries. Solid curves represent LEVs, and dotted lines represent TVs.

result, the TV mostly contributes to the generation of negative moments, which counteracts the LEV moment contribution.

At $t_2/T = 0.22$, figure 8(*b*) and the front view of figure 8(*e*) show that the LEV mostly detaches from the wing surface for the unswept wing except for a small portion near the wing tip, which stays attached. A similar flow structure was observed by Yilmaz & Rockwell (2012) for finite-span wings undergoing linear pitch-up motions, and by Son *et al.* (2022*a*) for high-aspect-ratio plunging wings. For the $\Lambda = 10°$ wing, this small

portion of the attached LEV shrinks (see the front view of figure 8*f*). The top portion of the LEV near the wing root is also observed to stay attached to the wing surface as compared to the $\Lambda = 0^\circ$ case. For the $\Lambda = 20^\circ$ wing, as shown by the front view of figure 8(*g*), the attached portion of the LEV near the wing tip shrinks further and almost detaches, while the top portion of the LEV also attaches to the wing surface, similar to that observed for $\Lambda = 10^\circ$. The shrinking of the LEV attached region near the wing tip as a function of the wing sweep is presumably caused by the decreased anchoring effect of the TV. The shrinking of the attached LEV could also be a result of an increased effective angle of attack. The side views of figures 8(*e–g*) show that the LEV moves towards the pivot axis at this time instant. The swept wing LEVs have slightly longer mean moment arms due to their attached portions near the wing root. This is more prominent for the $\Lambda = 20^\circ$ wing, potentially explaining the C_M of $\Lambda = 20^\circ$ exceeding the other two wings at t_2/T. The TV moves upwards and outwards with respect to the wing surface from t_1/T to t_2/T.

During the pitch reversal ($t_3/T = 0.30$), the LEV detaches further from the wing surface, and the TV also starts to detach. For the unswept wing, the LEV mostly aligns with the pivot axis except for the tip portion, which remains attached. For the $\Lambda = 10^\circ$ swept wing, the LEV also approximately aligns with the pivot axis, with both the root and the tip portions staying near the wing surface, forming a more prominent arch-like shape (see the front view of figure 8*f*) as compared to the previous time step. For the $\Lambda = 20^\circ$ wing, the root portion of the LEV stays attached and remains far in front of the pivot axis. The LEV detaches near the wing tip and joins with the detached TV, as shown by figure 8(*d*) and the front and side views of figure 8(*g*). The attachment of the LEV near the wing root, and the detachment of the TV near the wing tip, both contribute to a more positive C_M, as compared to the other two wings with lower sweep. The change of the LEV geometry as a function of the sweep angle can be associated with the arch vortices reported by Visbal & Garmann (2019). In their numerical study, it has been shown that for pitching unswept wings with free tips on both ends, an arch-type vortical structure began to form as the pitch reversal started (see their figure 6*c*). In our experiments, the wings have a free tip and an endplate (i.e. a wing–body junction, or symmetry plane). Therefore, the vortical structure shown in figure 8(*b*) is equivalent to one-half of the arch vortex. If we mirror the flow structures about the wing root (i.e. the endplate), then we can get a complete arch vortex similar to that observed by Visbal & Garmann (2019). For swept wings, we observe one complete arch vortex for both $\Lambda = 10^\circ$ (figure 8*c*) and $\Lambda = 20^\circ$ (figure 8*d*). Again, if we mirror the flow structures about the wing root, then there will be two arch vortices for each swept wing, agreeing well with the observation of Visbal & Garmann (2019) (see their figures 10*c* and 13*c*). Moreover, Visbal & Garmann (2019) reported that for swept wings, as Λ increases, the vortex arch moves towards the wing tip, which is also seen in our experiments (compare the front views of figures 8*e–g*).

3.7. *Insights obtained from moment partitioning*

We have shown in the previous subsection, § 3.6, that the aerodynamic moment is determined jointly by the LEV and TV dynamics. Specifically, the spatial locations and geometries of the LEV and TV, as well as the vortex strength, have a combined effect on the unsteady aerodynamic moment. To obtain further insights into this complex combined effect, we use the FMPM to analyse the three-dimensional flow fields.

As we discussed in § 2.4, the first step of applying the FMPM is to construct an 'influence potential' ϕ. We solve (2.6*a*,*b*) numerically using the MATLAB Partial Differential Equation Toolbox (finite element method, code available publicly

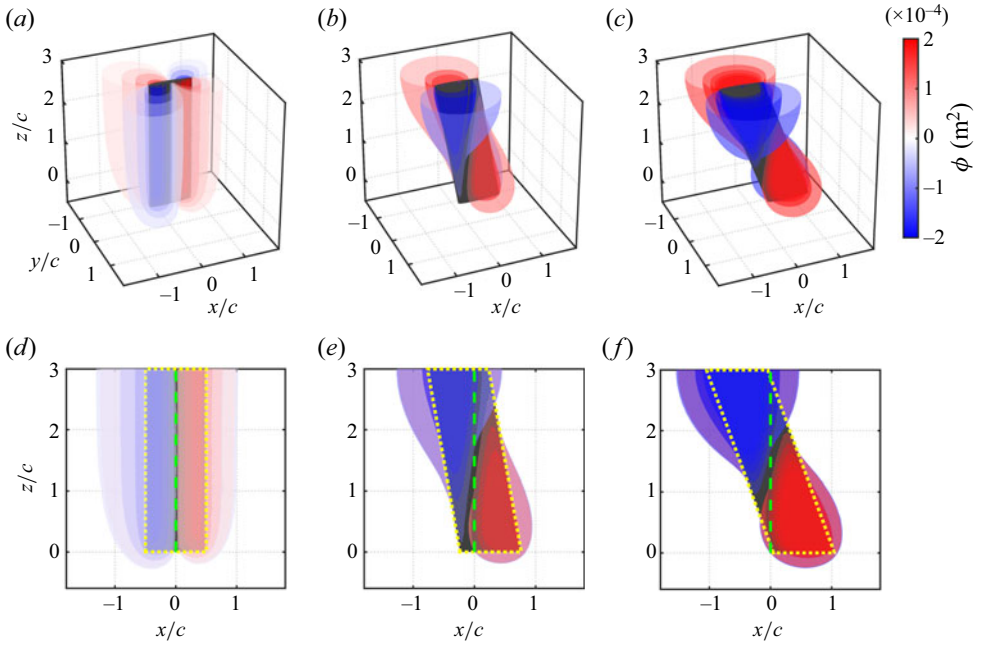

Figure 9. Iso-surface plots of three-dimensional influence potentials for (*a*) the $\Lambda = 0^\circ$ unswept wing, (*b*) the $\Lambda = 10^\circ$ swept wing, and (*c*) the $\Lambda = 20^\circ$ swept wing. (*d–f*) The corresponding side views, with the wing boundaries outlined by yellow dotted lines, and the pitching axes indicated by green dashed lines.

on MATLAB File Exchange; see supplementary material available at https://www.mathworks.com/matlabcentral/fileexchange/136194-force-and-moment-partitioning-influence-potential-solver-3d). We use a three-dimensional domain of size $10c \times 10c \times 20c$, and mesh resolution $0.02c$ on the surface of the wing and $0.1c$ on the outer domain. We visualize the calculated three-dimensional influence field ϕ for the $\Lambda = 0^\circ$, 10° and 20° wings using iso-ϕ surfaces in figures 9(*a–c*). Figures 9(*d–f*) illustrate the corresponding side views, with the wing boundaries outlined by yellow dotted lines, and the pitching axes indicated by green dashed lines. We see that for the unswept wing, the iso-ϕ surfaces show symmetry with respect to the pivot axis and the wing chord, resulting in a quadrant distribution of the influence field. The magnitude of ϕ peaks on the wing surface and decreases towards the far field. The slight asymmetry of ϕ with respect to the pitching axis (see figure 9*d*) is caused by the difference between the rounded leading edge and the sharp trailing edge of the NACA 0012 wing (see also the two-dimensional influence field reported in Zhu *et al.* 2023). The size of the iso-ϕ surfaces stays relatively constant along the wing span, except at the wing tip, where the surfaces wrap around and seal the tube.

As the sweep angle is increased to $\Lambda = 10^\circ$ and 20°, we see that the quadrant distribution of the influence field persists. However, the iso-ϕ surfaces form funnel-like shapes on the fore wing and teardrop shapes on the aft wing. This is caused by the variation of the effective pivot axis along the wing span. Figures 9(*e*) and 9(*f*) show that for swept wings, the negative ϕ regions extend over the entire chord near the wing root, even behind the pitching axis. Similarly, the positive ϕ regions (almost) cover the entire wing tip and even spill over in front of the pitching axis. As we will show next, this behaviour of the ϕ field for swept wings will result in some non-intuitive distributions of the aerodynamic

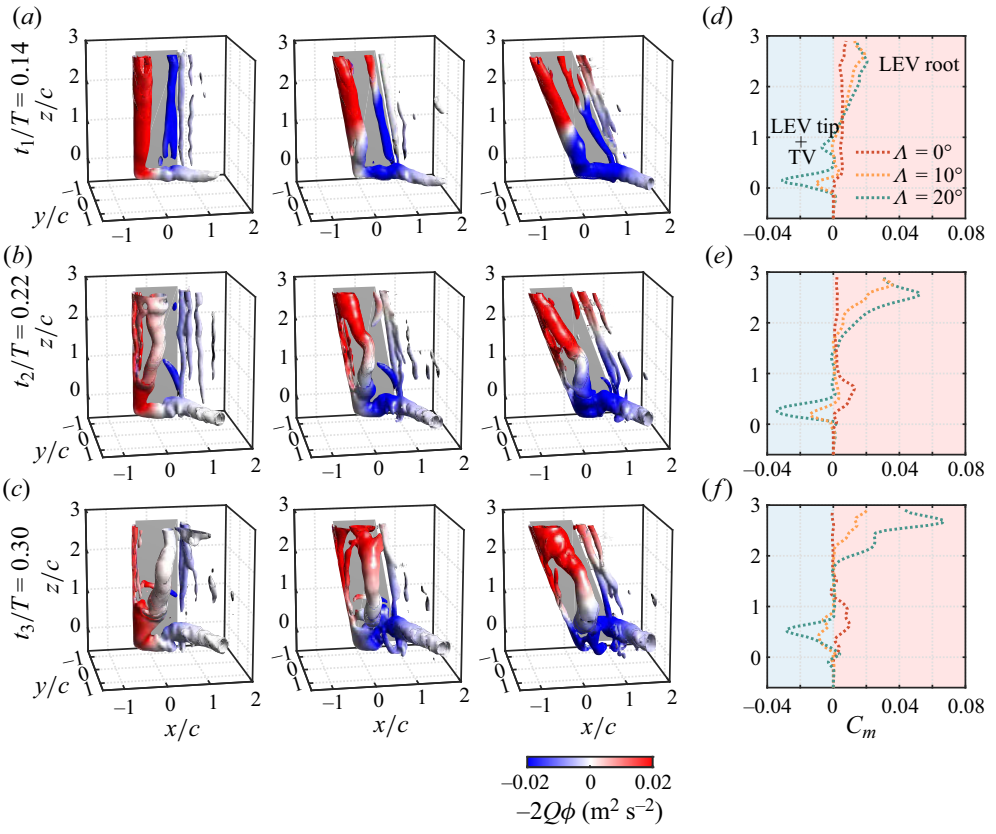

Figure 10. (*a–c*) Phase-averaged iso-Q surfaces ($Q = 50\,\mathrm{s}^{-2}$) for the $\Lambda = 0°$ unswept wing and the $\Lambda = 10°$ and 20° swept wings, coloured by the vorticity-induced moment density $-2Q\phi$ (m^2 s^{-2}), at $t_1/T = 0.14$, $t_2/T = 0.22$ and $t_3/T = 0.30$. Note that the wings and flow fields are rotated in the spanwise direction to maintain a zero angle of attack for a better view of the flow structures. (*d–f*) Spanwise distributions of the vorticity-induced moment for the three wings at the three representative time instants, obtained by integrating $-2Q\phi$ at different spanwise locations.

moment. In addition, the magnitude of the ϕ field is observed to increase with the sweep angle, due to the increase of the effective moment arm (Zhu, Mathai & Breuer 2021).

We multiply the three-dimensional Q field by the influence field ϕ and get the spanwise moment (density) distribution field $-2Q\phi$. To visualize the moment distributions, we recolour the same iso-Q surface plots shown in figure 8 with the moment density $-2Q\phi$, which are shown in figures 10(*a–c*). As before, the wings and flow fields are rotated by θ so that we are always looking from a viewpoint normal to the chord line, giving a better view of the flow structures. In these iso-Q surface plots, red regions indicate that the vortical structure induces a positive spanwise moment, whereas blue regions represent the generation of a negative spanwise moment. In between red and blue regions, white regions have zero contribution to the spanwise moment.

At $t_1/T = 0.14$ (figure 10*a*), as expected, we see that the entire LEV on the unswept wing is generating a positive moment. For the $\Lambda = 10°$ swept wing, however, the LEV generates a near-zero moment near the wing tip, and for the $\Lambda = 20°$ swept wing, the tip region of the LEV contributes a negative moment due to the non-conventional distribution of the ϕ field. The TV generates almost no moment for the unswept wing, but contributes a negative moment for the swept wings. The vortex tube formed near the trailing edge of

the wing surface contributes entirely to negative moments for the unswept wing, but its top portion starts to generate positive moments as the sweep angle increases. The contributions of each vortical structure on the moment generation for the three wings become clearer if we plot the spanwise distribution of the vorticity-induced moment.

By integrating the moment distribution field $-2Q\phi$ over the horizontal (x, y)-plane at each spanwise location z, we are able to obtain the spanwise distribution of the vorticity-induced moment, shown in figures 10(*d–f*). For the unswept wing ($\Lambda = 0^\circ$), figure 10(*d*) shows that the LEV generates a near-uniform positive moment across the span. As the sweep angle increases ($\Lambda = 10^\circ$), the LEV generates a higher positive moment near the wing root, and the TV starts to generate a negative moment. For the $\Lambda = 20^\circ$ wing, this trend persists. It is also interesting to see that the spanwise moment distribution curves for the three wings intersect around the mid-span, where the effective pivot axis coincides at the mid-chord. For the two swept wings, the more positive moments near the wing root counteract the negative LEV and TV contributions near the wing tip, resulting in a similar overall moment as compared to the unswept wing. The FMPM thus explains quantitatively why the three wings generate similar unsteady moments at this time instant (figure 8*a*).

At $t_2/T = 0.22$ (figure 10*b*), the LEV starts to detach and moves towards the pitching axis. As discussed in the previous subsection, § 3.6, the LEV forms a half-arch for the unswept wing, with only the tip region staying attached, and a complete arch for swept wings, with both the root and tip regions staying attached. These arch-like LEV geometries, together with the special shapes of the three-dimensional influence field, lead to some special distributions of the aerodynamic moments. For the unswept wing, the colour of the LEV becomes lighter as compared to the t_1/T case, indicating a decreasing contribution to positive moments. However, the attached portion of the LEV still generates a positive moment as it remains attached, close to the wing, and in front of the pitching axis. Comparing the two swept wing cases, the LEV for the $\Lambda = 20^\circ$ wing generates more positive moments near the wing root as compared to the $\Lambda = 10^\circ$ wing, due to the magnitude of the ϕ field (figure 9). The TVs for the three wings behave similarly to the cases at t_1/T. The aft wing vortex tube on the wing surface breaks into two smaller tubes. Because of their small volumes, we do not expect them to affect the total moment generation. Figure 10(*e*) shows that the large part of the LEV does not contribute to any moment generation for the unswept wing – only the tip region ($0 \leq z/c \leq 1$) generates positive moments. As compared to t_1/T, the LEV generates more positive moments near the wing root for the two swept wings, especially for the $\Lambda = 20^\circ$ wing, and the TV generates slightly more negative moments. The overall trend observed in figure 10(*e*) explains further the moment measurements shown in figure 8(*a*), where the $\Lambda = 20^\circ$ wing produces the highest C_M, followed by the $\Lambda = 10^\circ$ wing and then the unswept wing at t_2/T.

At $t_3/T = 0.30$ (figure 10*c*), the LEV detaches further from the wing surface. For the unswept wing, the LEV colour becomes even lighter. Comparing the temporal evolution of the LEV colour for the unswept wing, we see that the LEV generates progressivelylower positive moments, agreeing well with the decreasing moment measurement shown in figure 8(*a*). The LEV continues to generate positive moments near the root region and negative moments near the tip region for the $\Lambda = 10^\circ$ swept wing, although it is largely aligned with the pivot axis (see also the side view of figure 8*f*). This is again a result of the non-conventional funnel-shaped ϕ field near the wing root and the teardrop-like ϕ field near the wing tip (figures 9*b*,*e*). This trend persists for the $\Lambda = 20^\circ$ wing. However, the LEV generates more positive moments due to its shorter distance from the leading edge and the wing surface near the wing root. Moreover, the size of the LEV iso-Q surface also

becomes larger for the $\Lambda = 20^\circ$ wing as compared to the previous time steps, indicating a stronger LEV and thus a higher aerodynamic moment, which explains why the C_M of $\Lambda = 20^\circ$ peaks at approximately t_3/T in figure 8(a). This is also reflected in the spanwise moment plot in figure 10(f), where the LEV generates more positive moments for the $\Lambda = 20^\circ$ wing than the $\Lambda = 10^\circ$ wing. The TV again behaves similarly to the previous time steps for all three wings, although it becomes less coherent and detaches from the wing surface.

It is worth noting that the integral of $-2Q\phi$ over the (x, y)-plane (i.e. figures 10d–f) also includes contributions from other vortical structures. In figures 10(a–c), we can see that there are four main structures on each wing: the LEV, the TV, the trailing-edge vortex, and the vortex tube on the aft wing surface. Figure 9 shows that the amplitude of the influence field ϕ is zero near the trailing edge due to symmetry. This means that the contribution to the moment by the trailing-edge vortex is negligible, because $-2Q\phi$ approaches zero in this region and makes no contribution to the integrand. The aft wing vortex tube is small in size compared to the LEV and TV. In addition, it is not as coherent, because it breaks down at $t_2/T = 0.22$. Therefore, we would expect its contribution to the integral to be small as well.

In summary, the FMPM enables us to associate the complex three-dimensional vortex dynamics with the corresponding vorticity-induced moments, and explains quantitatively the mechanisms behind the observed differences in the unsteady moment generation, which further drives the pitching motion of these swept wings. These insightful analyses would not have been possible without the FMPM.

4. Conclusion

In this experimental study, we have explored the nonlinear flow-induced oscillations and three-dimensional vortex dynamics of cyber-physically mounted pitching unswept and swept wings, with the pitching axis passing through the mid-chord point at the mid-span plane, and with the sweep angle varied from 0° to 25°. At a constant flow speed, a prescribed high inertia and a small structural damping, we adjusted the wing stiffness to study systematically the onset and extinction of large-amplitude flow-induced oscillations. For the current selections of the pitching axis location and the range of the sweep angle, the amplitude response revealed subcritical Hopf bifurcations for all the unswept and swept wings, with a clustering behaviour for the Hopf point and a non-monotonic saddle-node point as a function of the sweep angle. The flow-induced oscillations have been correlated with the structural oscillation mode, where the oscillations are dominated by the inertial behaviour of the wing. For swept wings with high sweep angles, a hybrid oscillation mode, namely the structural-hydrodynamic mode, has been observed and characterized, in which the oscillations were regulated by both the inertial moment and the fluid moment. The onset of flow-induced oscillations (i.e. the Hopf point) has been shown to depend on the static characteristics of the wing. The non-monotonic trend of the saddle-node point against the sweep angle can be attributed to the non-monotonic power transfer between the ambient fluid and the elastic mount, which depends further on the amplitude and phase of the unsteady aerodynamic moment. Force and moment measurements have shown that, perhaps surprisingly, the wing sweep has a minimal effect on the aerodynamic forces, and it was therefore inferred that the wing sweep modulates the aerodynamic moment by affecting the moment arm. Phase-averaged three-dimensional flow structures measured using stereoscopic PIV have been analysed to characterize the dynamics of the LEV and TV. Finally, by employing the force and moment partitioning method (FMPM),

we have correlated successfully the complex LEV and TV dynamics with the resultant aerodynamic moment in a quantitative manner.

In addition to reporting new observations and providing physical insights on the effects of moderate wing sweep in large-amplitude aeroelastic oscillations, the present study can serve as a source of validation data for future theoretical/computational models. Furthermore, the optimal sweep angle ($\Lambda = 10^\circ$) observed for promoting flow-induced oscillations may have engineering implications. For example, one should avoid this sweep angle for aero-structure designs to stay away from aeroelastic instabilities. On the other hand, potentially this angle could be employed for developing higher-efficiency flapping-foil energy-harvesting devices. Finally, the use of FMPM to analyse (especially three-dimensional) flow fields obtained from PIV experiments has shown great utility, and the results demonstrated further the powerful capability of this emerging method to provide valuable physical insights into vortex-dominated flows, paving the way for more applications of this method to data from future experimental and numerical studies.

Supplementary material and movie. Supplementary material is available at https://www.mathworks.com/matlabcentral/fileexchange/136194-force-and-moment-partitioning-influence-potential-solver-3d. Supplementary movie is available at https://doi.org/10.1017/jfm.2023.925.

Funding. This work is funded by the Air Force Office of Scientific Research, grant FA9550-21-1-0462, managed by Dr G. Abate. We acknowledge helpful discussions with R. Mittal, K. Menon and S. Kumar.

Declaration of interests. The authors report no conflict of interest.

Author ORCIDs.
Yuanhang Zhu https://orcid.org/0000-0002-2080-1142;
Kenneth Breuer https://orcid.org/0000-0002-5122-2231.

References

Beatus, T. & Cohen, I. 2015 Wing-pitch modulation in maneuvering fruit flies is explained by an interplay between aerodynamics and a torsional spring. *Phys. Rev.* E **92** (2), 022712.

Beem, H.R., Rival, D.E. & Triantafyllou, M.S. 2012 On the stabilization of leading-edge vortices with spanwise flow. *Exp. Fluids* **52** (2), 511–517.

Bergou, A.J., Xu, S. & Wang, Z.J. 2007 Passive wing pitch reversal in insect flight. *J. Fluid Mech.* **591**, 321–337.

Birch, J.M. & Dickinson, M.H. 2001 Spanwise flow and the attachment of the leading-edge vortex on insect wings. *Nature* **412** (6848), 729–733.

Borazjani, I. & Daghooghi, M. 2013 The fish tail motion forms an attached leading edge vortex. *Proc. R. Soc.* B **280** (1756), 20122071.

Bottom II, R.G., Borazjani, I., Blevins, E.L. & Lauder, G.V. 2016 Hydrodynamics of swimming in stingrays: numerical simulations and the role of the leading-edge vortex. *J. Fluid Mech.* **788**, 407–443.

Boudreau, M., Dumas, G., Rahimpour, M. & Oshkai, P. 2018 Experimental investigation of the energy extraction by a fully-passive flapping-foil hydrokinetic turbine prototype. *J. Fluids Struct.* **82**, 446–472.

Chiereghin, N., Bull, S., Cleaver, D.J. & Gursul, I. 2020 Three-dimensionality of leading-edge vortices on high aspect ratio plunging wings. *Phys. Rev. Fluids* **5** (6), 064701.

Dimitriadis, G. & Li, J. 2009 Bifurcation behavior of airfoil undergoing stall flutter oscillations in low-speed wind tunnel. *AIAA J.* **47** (11), 2577–2596.

Dowell, E.H., Curtiss, H.C., Scanlan, R.H. & Sisto, F. 1989 *A Modern Course in Aeroelasticity*. Springer.

Eldredge, J.D. & Jones, A.R. 2019 Leading-edge vortices: mechanics and modeling. *Annu. Rev. Fluid Mech.* **51**, 75–104.

Ellington, C.P., van den Berg, C., Willmott, A.P. & Thomas, A.L.R. 1996 Leading-edge vortices in insect flight. *Nature* **384** (6610), 626.

Gursul, I. & Cleaver, D. 2019 Plunging oscillations of airfoils and wings: progress, opportunities, and challenges. *AIAA J.* **57** (9), 3648–3665.

HARTLOPER, C., KINZEL, M. & RIVAL, D.E. 2013 On the competition between leading-edge and tip-vortex growth for a pitching plate. *Exp. Fluids* **54** (1), 1447.
HOVER, F.S., MILLER, S.N. & TRIANTAFYLLOU, M.S. 1997 Vortex-induced vibration of marine cables: experiments using force feedback. *J. Fluids Struct.* **11** (3), 307–326.
HUNT, J.C.R., WRAY, A.A. & MOIN, P. 1988 Eddies, streams, and convergence zones in turbulent flows. In *Center for Turbulence Research*, pp. 193–208.
JAFFERIS, N.T., HELBLING, E.F., KARPELSON, M. & WOOD, R.J. 2019 Untethered flight of an insect-sized flapping-wing microscale aerial vehicle. *Nature* **570** (7762), 491–495.
JEONG, J. & HUSSAIN, F. 1995 On the identification of a vortex. *J. Fluid Mech.* **285**, 69–94.
JONES, R.T. 1947 Effects of sweepback on boundary layer and separation. *Tech. Rep.* 1042. NACA.
KIM, D. & GHARIB, M. 2010 Experimental study of three-dimensional vortex structures in translating and rotating plates. *Exp. Fluids* **49**, 329–339.
KING, J.T., KUMAR, R. & GREEN, M.A. 2018 Experimental observations of the three-dimensional wake structures and dynamics generated by a rigid, bioinspired pitching panel. *Phys. Rev. Fluids* **3** (3), 034701.
LENTINK, D., MÜLLER, U.K., STAMHUIS, E.J., DE KAT, R., VAN GESTEL, W., VELDHUIS, L.L.M., HENNINGSSON, P., HEDENSTRÖM, A., VIDELER, J.J. & VAN LEEUWEN, J.L. 2007 How swifts control their glide performance with morphing wings. *Nature* **446** (7139), 1082–1085.
LI, J., WANG, Y., GRAHAM, M. & ZHAO, X. 2020*a* Vortex moment map for unsteady incompressible viscous flows. *J. Fluid Mech.* **891**, A13.
LI, J. & WU, Z.-N. 2018 Vortex force map method for viscous flows of general airfoils. *J. Fluid Mech.* **836**, 145–166.
LI, J., ZHAO, X. & GRAHAM, M. 2020*b* Vortex force maps for three-dimensional unsteady flows with application to a delta wing. *J. Fluid Mech.* **900**, A36.
LONG, J.H. & NIPPER, K.S. 1996 The importance of body stiffness in undulatory propulsion. *Am. Zool.* **36** (6), 678–694.
MACKOWSKI, A.W. & WILLIAMSON, C.H.K. 2011 Developing a cyber-physical fluid dynamics facility for fluid–structure interaction studies. *J. Fluids Struct.* **27** (5–6), 748–757.
MCCROSKEY, W.J. 1982 Unsteady airfoils. *Annu. Rev. Fluid Mech.* **14** (1), 285–311.
MENON, K., KUMAR, S. & MITTAL, R. 2022 Contribution of spanwise and cross-span vortices to the lift generation of low-aspect-ratio wings: insights from force partitioning. *Phys. Rev. Fluids* **7** (11), 114102.
MENON, K. & MITTAL, R. 2019 Flow physics and dynamics of flow-induced pitch oscillations of an airfoil. *J. Fluid Mech.* **877**, 582–613.
MENON, K. & MITTAL, R. 2021*a* On the initiation and sustenance of flow-induced vibration of cylinders: insights from force partitioning. *J. Fluid Mech.* **907**, A37.
MENON, K. & MITTAL, R. 2021*b* Quantitative analysis of the kinematics and induced aerodynamic loading of individual vortices in vortex-dominated flows: a computation and data-driven approach. *J. Comput. Phys.* **443**, 110515.
MENON, K. & MITTAL, R. 2021*c* Significance of the strain-dominated region around a vortex on induced aerodynamic loads. *J. Fluid Mech.* **918**, R3.
MORICHE, M., FLORES, O. & GARCÍA-VILLALBA, M. 2017 On the aerodynamic forces on heaving and pitching airfoils at low Reynolds number. *J. Fluid Mech.* **828**, 395–423.
MORSE, T.L. & WILLIAMSON, C.H.K. 2009 Prediction of vortex-induced vibration response by employing controlled motion. *J. Fluid Mech.* **634**, 5–39.
MULLENERS, K. & RAFFEL, M. 2012 The onset of dynamic stall revisited. *Exp. Fluids* **52** (3), 779–793.
NEGI, P.S., HANIFI, A. & HENNINGSON, D.S. 2021 On the onset of aeroelastic pitch-oscillations of a NACA0012 wing at transitional Reynolds numbers. *J. Fluids Struct.* **105**, 103344.
ONOUE, K. & BREUER, K.S. 2016 Vortex formation and shedding from a cyber-physical pitching plate. *J. Fluid Mech.* **793**, 229–247.
ONOUE, K. & BREUER, K.S. 2017 A scaling for vortex formation on swept and unswept pitching wings. *J. Fluid Mech.* **832**, 697–720.
ONOUE, K., SONG, A., STROM, B. & BREUER, K.S. 2015 Large amplitude flow-induced oscillations and energy harvesting using a cyber-physical pitching plate. *J. Fluids Struct.* **55**, 262–275.
POLHAMUS, E.C. 1971 Predictions of vortex-lift characteristics by a leading-edge suction analogy. *J. Aircraft* **8** (4), 193–199.
QUARTAPELLE, L. & NAPOLITANO, M. 1983 Force and moment in incompressible flows. *AIAA J.* **21** (6), 911–913.
QUINN, D. & LAUDER, G. 2021 Tunable stiffness in fish robotics: mechanisms and advantages. *Bioinspir. Biomim.* **17** (1), 011002.
RAO, S.S. 1995 *Mechanical Vibrations*. Addison-Wesley.

RIBEIRO, J.H.M., YEH, C.-A., ZHANG, K. & TAIRA, K. 2022 Wing sweep effects on laminar separated flows. *J. Fluid Mech.* **950**, A23.

RIVAL, D.E., KRIEGSEIS, J., SCHAUB, P., WIDMANN, A. & TROPEA, C. 2014 Characteristic length scales for vortex detachment on plunging profiles with varying leading-edge geometry. *Exp. Fluids* **55** (1), 1–8.

SHYY, W., AONO, H., CHIMAKURTHI, S.K., TRIZILA, P., KANG, C.-K., CESNIK, C.E.S. & LIU, H. 2010 Recent progress in flapping wing aerodynamics and aeroelasticity. *Prog. Aerosp. Sci.* **46** (7), 284–327.

SON, O., GAO, A.-K., GURSUL, I., CANTWELL, C.D., WANG, Z. & SHERWIN, S.J. 2022*a* Leading-edge vortex dynamics on plunging airfoils and wings. *J. Fluid Mech.* **940**, A28.

SON, O., WANG, Z. & GURSUL, I. 2022*b* Dynamics of tip vortices on plunging wings. *Aerosp. Sci. Technol.* **128**, 107761.

STROGATZ, S.H. 1994 *Nonlinear Dynamics and Chaos: With Applications to Physics, Biology, Chemistry, and Engineering*. Perseus Books.

SU, Y & BREUER, K.S. 2019 Resonant response and optimal energy harvesting of an elastically mounted pitching and heaving hydrofoil. *Phys. Rev. Fluids* **4** (6), 064701.

TAIRA, K. & COLONIUS, T. 2009 Three-dimensional flows around low-aspect-ratio flat-plate wings at low Reynolds numbers. *J. Fluid Mech.* **623**, 187–207.

TONG, R., WU, Z., CHEN, D., WANG, J., DU, S., TAN, M. & YU, J. 2022 Design and optimization of an untethered high-performance robotic tuna. *IEEE/ASME Trans. Mechatron.* **27** (5), 4132–4142.

VISBAL, M.R. & GARMANN, D.J. 2019 Effect of sweep on dynamic stall of a pitching finite-aspect-ratio wing. *AIAA J.* **57** (8), 3274–3289.

WANG, Z.J. 2005 Dissecting insect flight. *Annu. Rev. Fluid Mech.* **37**, 183–210.

WOJCIK, C.J. & BUCHHOLZ, J.H.J. 2014 Vorticity transport in the leading-edge vortex on a rotating blade. *J. Fluid Mech.* **743**, 249.

WONG, J.G., KRIEGSEIS, J. & RIVAL, D.E. 2013 An investigation into vortex growth and stabilization for two-dimensional plunging and flapping plates with varying sweep. *J. Fluids Struct.* **43**, 231–243.

WONG, J.G. & RIVAL, D.E. 2015 Determining the relative stability of leading-edge vortices on nominally two-dimensional flapping profiles. *J. Fluid Mech.* **766**, 611.

WU, K.S., NOWAK, J. & BREUER, K.S. 2019 Scaling of the performance of insect-inspired passive-pitching flapping wings. *J. R. Soc. Interface* **16** (161), 20190609.

XIAO, Q. & ZHU, Q. 2014 A review on flow energy harvesters based on flapping foils. *J. Fluids Struct.* **46**, 174–191.

YILMAZ, T.O. & ROCKWELL, D. 2012 Flow structure on finite-span wings due to pitch-up motion. *J. Fluid Mech.* **691**, 518.

YOUNG, J., LAI, J.C.S. & PLATZER, M.F. 2014 A review of progress and challenges in flapping foil power generation. *Prog. Aerosp. Sci.* **67**, 2–28.

YUAN, W., POIREL, D., WANG, B. & BENAISSA, A. 2015 Effect of freestream turbulence on airfoil limit-cycle oscillations at transitional Reynolds numbers. *J. Aircraft* **52** (4), 1214–1225.

ZHANG, C., HEDRICK, T.L. & MITTAL, R. 2015 Centripetal acceleration reaction: an effective and robust mechanism for flapping flight in insects. *PLoS ONE* **10** (8), e0132093.

ZHANG, K., HAYOSTEK, S., AMITAY, M., BURTSEV, A., THEOFILIS, V. & TAIRA, K. 2020*a* Laminar separated flows over finite-aspect-ratio swept wings. *J. Fluid Mech.* **905**, R1.

ZHANG, K., HAYOSTEK, S., AMITAY, M., HE, W., THEOFILIS, V. & TAIRA, K. 2020*b* On the formation of three-dimensional separated flows over wings under tip effects. *J. Fluid Mech.* **895**, A9.

ZHANG, K. & TAIRA, K. 2022 Laminar vortex dynamics around forward-swept wings. *Phys. Rev. Fluids* **7** (2), 024704.

ZHONG, Q., HAN, T., MOORED, K.W. & QUINN, D.B. 2021*a* Aspect ratio affects the equilibrium altitude of near-ground swimmers. *J. Fluid Mech.* **917**, A36.

ZHONG, Q., ZHU, J., FISH, F.E., KERR, S.J., DOWNS, A.M., BART-SMITH, H. & QUINN, D.B. 2021*b* Tunable stiffness enables fast and efficient swimming in fish-like robots. *Sci. Robot.* **6** (57), eabe4088.

ZHU, Y., LEE, H., KUMAR, S., MENON, K., MITTAL, R. & BREUER, K. 2023 Force moment partitioning and scaling analysis of vortices shed by a 2D pitching wing in quiescent fluid. *Exp. Fluids* **64** (10), 158.

ZHU, Y., MATHAI, V. & BREUER, K. 2021 Nonlinear fluid damping of elastically mounted pitching wings in quiescent water. *J. Fluid Mech.* **923**, R2.

ZHU, Y., SU, Y. & BREUER, K. 2020 Nonlinear flow-induced instability of an elastically mounted pitching wing. *J. Fluid Mech.* **899**, A35.

ZURMAN-NASUTION, A.N., GANAPATHISUBRAMANI, B. & WEYMOUTH, G.D. 2021 Fin sweep angle does not determine flapping propulsive performance. *J. R. Soc. Interface* **18** (178), 20210174.